SURE 静岡大学学術リポジトリ
Shizuoka University REpository

Growth of 4-6 semiconductors for optical device applications

メタデータ	言語: en
	出版者: Shizuoka University
	公開日: 2012-03-13
	キーワード (Ja):
	キーワード (En):
	作成者: Cao, Daoshe
	メールアドレス:
	所属:
URL	https://doi.org/10.14945/00006458

DOCTOR THESIS

Growth of IV-VI Semiconductors for Optical Device Applications

Daoshe Cao

Graduate School of Science and Technology

SHIZUOKA UNIVERSITY

Supervisor: Prof. Akihiro Ishida

July 2010

静岡大学

創造科学技術大学院

博士論文

光デバイス応用へ向けた IV-VI 族半導体の成長

曹　道社

浜松　2010

Abstract

Novel lasers and detectors in the mid-infrared wavelength region are proposed, and the device structures were grown by hot wall epitaxy system prepared for device applications. The mid-infrared range (3-30μm) is technologically important for night vision, gas sensor, and optical spectroscopy, due to the strong absorption lines of various gases in this range.

New electrically pumped vertical cavity surface emitting lasers (VCSELs), which based on conductive IV-VI semiconductors, were designed, and grown on BaF_2(111) substrate. The laser structure consists of *p*- and *n*-type PbTe/PbS high reflectivity Bragg mirrors, and non-dope PbSe as active layer. Optical transmission and reflection spectra of the laser structure designed for 6μm in output wavelength was measured. From the temperature dependence of optical transmission spectra, absorption at resonant wavelength (6μm) was observed at 150K, as expected from the band gap of PbSe.

EuTe/PbTe quantum cascade structures were deposited on KCl (100) substrate by hot wall epitaxy system. XRD measurements of the structure exhibited many number of satellite peaks, which confirmed a high quality EuTe/PbTe quantum cascade structure. Intersubband absorption in this

structure was observed at room temperature in normal incident transmission spectra measured by Fourier transform infrared (FTIR) spectroscopy. This structure gives the possibility of fabrication of novel devices, such as vertical cavity surface emitting quantum cascade laser (VCSEQCL) or intersubband image sensor at normal incidence.

Resonant cavity detector (RCD) structure, which has sensitivity for special wavelength designed, was also proposed using the n-PbSrSe -PbSe-p-PbSrSe active region between *p-*, *n-* PbTe/PbS Bragg resonator. Optical transmission spectra of the RCD structure was measured and discussed.

Contents

1 Introduction..1

1.1 General introduction 1

1.2 Lead salt lasers...2

1.3 IV-VI photo detectors..3

1.4 Motivation..4

2 Material properties...8

2.1 Crystal lattice..8

2.2 Band structure..10

2.3 Doping 14

3 Growth Technology...21

3.1 Hot wall epitaxy..21

3.2 Source Tube...24

3.3 Substrates..24

3.3.1 KCl substrate...24

3.3.2 BaF_2 substrate...25

4 Characterization Methods..27

4.1 Optical property...27

4.2 X-ray diffraction...29

4.3 Hall effect measurement 34

4.3.1 The Hall effect and the Lorentz force........................ 34

4.3.2 Van der Pauw method for the Hall measurements............36

5 Design and Fabrication of Electrical Pumped VCSEL.........40

5.1 Introduction...40

5.2Theory of VCSEL...41

5.3 Mirror materials..45

5.4 Preparing PbTe and PbS films.....................................45

5.5 PbTe/PbS multiple mirror...47

5.6 VCSEL structure..50

5.7 Etching technique for device fabrication.........................55

5.8 Summary.....59

6 Infrared detectors.....63
6.1 Introduction.....63
6.2 Classification of IR detectors.....65
6.3Introduction of photovoltaic infrared detector based on intersubband absorption.....67
6.4Intersubband absorption in EuTe/PbTe quantum cascade structure.....71
6.5Resonant cavity enhance detector structure base on IV-VI semiconductors.....74
6.5.1 Design of RCD.....74
6.5.2 Fabrication of RCD.....78
6.6 Summary.....80

7 Conclusions.....83

Appendix.....85
Acknowledgements.....86
List of publication.....87

Chapter 1
Introduction

1.1 General introduction

The infrared radiation (IR) is the region of the electromagnetic spectrum with wavelength longer than visible light (400 to 710nm) but shorter than microwaves (1 mm to 30 cm). It is often divided in three sub regions: the near infrared (NIR) going from 710 nm to 2.5μm.The mid-infrared (MIR) from 2.5 to 25 μm, and the far infrared (FIR) from 25μm to 1mm.

The near-infrared radiation interacts with matter essentially the same way as visible light. This spectral range has a major technological importance because it is a standard for optical telecommunications and data storage. Nowadays, it is the most developed among the three IR sub regions in terms of available laser sources and detectors. High performance NIR diode laser are easily available and inexpensive because of mass-fabrication. According to Ref.1, 396 million units have been sold during year 2004, compared to 337 millions of visible diode laser and 131 millions of all other types of lasers.

The far-infrared to terahertz region is at the boundary between light and microwaves. Coherent THz local oscillators are important in astronomy since most of the interstellar dust clouds emit in this region. Other application of THz radiation including imaging in the field of biology, medicine, and home land security and absorption spectroscopy. However, the development of these applications is slow because of the lack of compact, powerful sources of coherent radiation in this region. This situation may change with

the ongoing development of THz quantum cascade lasers if cryogenic free operation can be achieved.

The MIR range, sometimes called the finger-print region of the electromagnetic spectrum, is of enormous scientific and technological interest since many molecules have their fundamental rotational and vibrational absorption bands in this range. The MIR absorption spectrum is very specific to the structure of a particular molecule, allowing highly selective detection. In addition, since these absorption lines are very strong (several order of magnitude stronger than the overtone and combination bands in the NIR), concentrations in the parts-per-billion (ppb) to parts-per-trillion (ppt) ranges can be detected using relatively compact laser- based sensors. Fast, sensitive, and selective chemical sensors are needed in numerous applications. In industrial process control they are used for detection of contamination in semiconductor fabrication lines and for plasma monitoring, in law enforcement for drug and explosive detection, in automotive industry for engine exhaust analysis, in environmental science for pollution monitoring, in medical diagnostics for exhaled breath analysis.

Another interesting feature of the MIR is the atmospheric transmission windows between 3-5 μm and 8-12μm which enable free-space optical communications, remote sensing, and thermal imaging. High power lasers in the 3-5μm range will also enable the development of infrared counter-measures for homeland security.

1.2 Lead salt lasers

The IV-VI lead salt semiconductors are interesting materials for MIR optoelectronics [2], detectors, and thermal device [3, 4]. In these materials the direct band gap located at the L points of the Brillouin zone. In addition, the conduction band and valence band are

quite similar, so that electrons and holes have comparable effective masses. This property results in a two orders of magnitude smaller Auger recombination rate for the Pb salts compared to III-V material with equal band gap energy, allowing maintaining population inversion and thus lasing operation, at higher temperature [5].

Laser diode based on this material system has been developed for operation at wavelengths from 3 to 30 μm. The active regions are usually double heterostructures and are grown by MBE or HWE [6-9]. The active material is PbSe, PbTe or PbS and the band gap of cladding material is adjusted by addition of Cd, Sn, Eu or Yb that leads to strong shift of band gap with little lattice constant variation. Because of the small Auger recombination rate, laser operation up to 60℃ at 5μm has been achieved in pulse mode [10], but, because of the low thermal conductivity of those materials, CW operation was observed only up to 223K [11], and thus this laser required liquid nitrogen cooling. The typical output powers are of the order of hundreds of microwatts. Although single-mode distributed feedback devices have been demonstrated, the limited market has not allowed the necessary investments to turn them into a commercial product. The standard devices are Fabry-Perot chips tuned by current or temperature. The typical tuning range is 1000-1200 cm^{-1} by varying the device temperature, or several tens of cm^{-1} by changing the injection current. In the present work, fabrication and characterize optical properties of IV-VI narrow gap compounds VCSEL structure for the 5-7μm wavelength range at low temperature are described.

1.3 IV-VI photodetectors

Infrared devices for the thermal 3μm to 12μm wavelength range fabricated in narrow gap semiconductors exhibit highest sensitivity at a given operation temperature. With

single crystal IV-VI materials, cut-off wavelengths covering the whole thermal infrared range from about 3μm up to above 30μm are possible. IV-VI semiconductors infrared photodetectors are realized in photovoltaic and photoconductive mode. The latter are commercially available [12-14]. Photo diodes and photo diode arrays have been realized using various designs [15]. We will describe EuTe/PbTe infrared detector using intersubband absorption property in this thesis.

1.4 Motivation

The main purpose of this work was to grow and characterize IV-VI semiconductor thin layers, and applications for mid-infrared devices. Narrow gap IV-VI semiconductors, mainly binary PbTe, PbSe and PbS, were epitaxially grown by hot wall epitaxy on (111) oriented BaF_2 and (100) oriented KCl. Owing to their direct narrow band gaps in the range of 0.2~0.3 eV, the main applications are mid-infrared optoelectronic devices such as lasers and detectors. In this thesis, we will focus on design and fabrication of electrically pumped vertical cavity surface emitting laser structures and detectors based on IV-VI semiconductors in the mid-infrared spectra range.

The present PhD thesis is organized as follows:

- Chapter 2 describes material properties of the lead chalcogenide compounds (means PbTe, PbS and PbSe).
- Chapter 3 includes basics of growth method: Hot wall epitaxy system, and substrate.
- Chapter 4 describes basic description and characteristic of experimental techniques used for characterization of grown samples.

- Chapter 5 describes applications of IV-VI compounds for optoelectronic devices. Basic theoretical of VCSELs, original results on electrical pumped VCSEL structure based on IV-VI semiconductors, and the fabrication of device processing are described.
- Chapter 6 describes the result of normal incident intersubband absorption in EuTe/PbTe quantum cascade structure for infrared detector application; and resonant cavity enhance detector structure base on IV-VI semiconductors are also proposed.
- Chapter 7 is summary of this work result and conclusions are given.

References

1. Kincade, Kathy and Stephen Anderson, Laser Focuse World, 2005,41,1.
2. A.Ishida, and H. Fujiyasu, laser application of IV-VI semiconductors, in Lead chalcogenides physics and application, Taylor and Francis.
3. H. Zogg, S. Blunier, T. Hoshino, C. Maissen, J. Masek, and A. N .Tiwari, IEEE Trans. Electron Devices, 1991, ED38 , p 1110.
4. A. Ishida, D.S.Cao, S.Morioka, M. Veis, Y. Inoue, and T.Kita, Appl. Phy. Letter, 2008, 92, p. 182105.
5. M.Tacke, Phil. Trans. R. Soc. A , 2001, 359, 547.
6. R. Rosman, A.Katzir, P. Norton, K. H. Bachem and H.M.Peier, IEEE J. Quantum Electron., 1987, QE-23,94.
7. B. Spanger, U. Schiessl, A.Lambrecht, H. Bottner, and M. Tacke, Appl. Phys. Letter, 1988, 54, 2582.
8. K.Murase, S. Shinomura, S. Takaoka, A. Ishida, and H. Fujiyasu, Superlattices and Microstructures, 1985,1,177.
9. K. Shinohara, Y.Nishijima, H. Eba, A.Ishida, and H. Fujiyasu, Appl. Phys. Letter, 1985,47,1184.
10. U. P. Schiessl and J. Rohr, Infrared Phys. Technol., 1999, 40, 325.
11. Z. Feit , M. McDonald, R. J. Woods, V. Archambault and P. Mak, Appl. Phys. Letter, 1996, 68,738.
12. Hamamatsu company, Japan, www.hamamatsu.com.
13. Calsensors, Santa Rosa, CA, USA, www.calsensors.com.
14. Juson Technologies, Montgomeryville, PA, USA, www.judtech.com.
15. H. Zogg, K. Alchalabi, D. Zimin, K. Kellermann, IEEE Trans. Electron

Devices, 2003,50,208.

Chapter 2
Material properties

The lead chalcogenides such as PbTe, PbSe and PbS together with other IV-VI type compounds possess an exceptional set of physical features described in many reviews [1-6]. A relatively complete list of reference papers published up to 1968 is available in Ref.2. In order to limit the number of references in this chapter, we will mainly explain IV-VI semiconductor crystal lattice, band structure and doping methods.

2.1 Crystal lattice

Lead chalcogenides have NaCl-type crystal lattices of the Fm3m symmetry class. The unit cell is a face-centered cubic lattice. Each site of the lattice is an inversion center, and the coordination number for all atoms is six. The Brillouin zone of the lead chalcogenides is shown in Fig. 2.1[2]. The lattice constant *a* and the size of cubic cell, is given in Tab. 2.1. Concerning mechanical properties, the lead chalcogenide crystals are rather brittle and easily cleaved along the (100) planes at relatively low temperatures. The elastic properties are characterized by three independent elastic moduli c_{11}, c_{12} and c_{44}, also shown in table1 [7-10].

The dielectric constants of the chalcogenides are rather high, and the high-frequency ε_∞ and static ε_0 dielectric permittivities strongly differ. The magnitudes of ε_0 essentially depend on temperature; the room temperature values [3, 11] are shown in Tab 2.1 together with ε_∞.

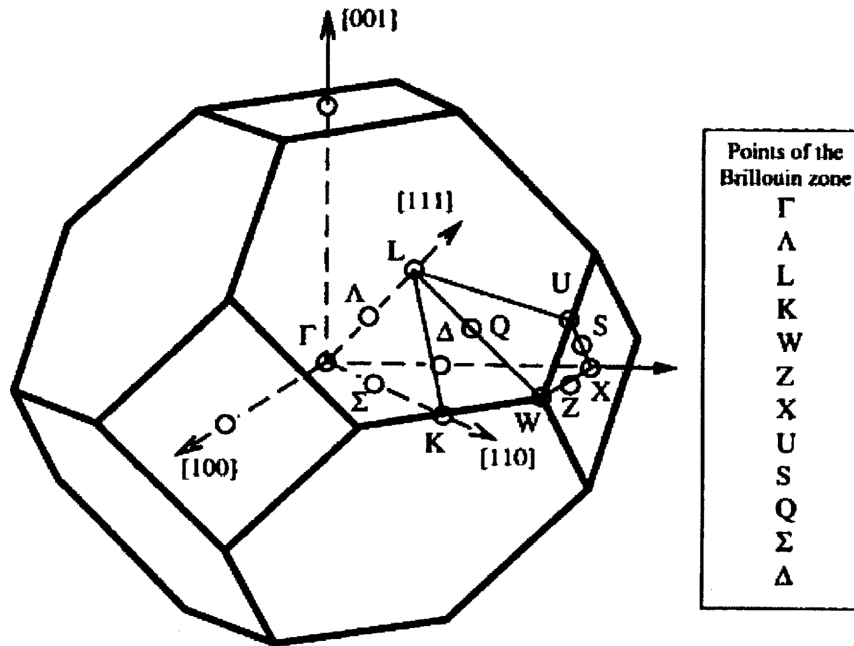

Figure2.1 Brillouin zone of a face-centered cubic lattice (PbTe) (Ref.2).

Table 2.1 lattice parameters of the lead chalcogenides.

Parameter	PbTe	PbSe	PbS
a , Å	6.46	6.12	5.94
ε_{∞}	33	23	17
ε_{0} (300k)	414	204	169
$C_{11}, 10^{10}\ N/m^2$	10.53	12.37	12.6
$C_{12}, 10^{10}\ N/m^2$	0.70	1.93	1.6
$C_{44}, 10^{10}\ N/m^2$	1.32	1.59	1.7
V_{LO}, THz	3.42(300K)	3.99(4.2K)	6.14(300K)
V_{TO}, THz	0.965(300K)		1.96(300K)
	0.564(4.2K)	1.32(1.4K)	
n (refractive index)	5.6	5	4

The refractive index of IV-VI materials shown in Tab.2.1. In the case of light, the refractive index is concerned with ε_{∞} as follow:

$$n = \sqrt{\varepsilon_{\infty}\mu_r} \qquad (2.1)$$

Where μ_r is its relative permeability. For most naturally occurring materials, μ_r is very close to 1 at optical frequencies [51]. Therefore n is approximately $\sqrt{\varepsilon_{\infty}}$.

The electron properties of the IV-VI semiconductors are close to those of the V group elements because both types of crystals have an equal mean number of electrons per atom. If both atoms of the cell are considered as chemically equivalent, the crystal lattices are simple cubic, and the difference between atoms of the IV and VI group, the crystal becomes a narrow gap semiconductor; the metallic contribution to the total binding, however, remains large. Thus, the binding in the crystals in question is a complicated interplay of ionic, covalent, and metallic contributions [14-20]. The idea of the metallic component of the chemical binding is important in the problem of instability of the VI-VI cubic lattices [13-16]. Inasmuch as the small average energy gap is purely ionic in the NaCl-type lattice [13-16], the binding of the lead chalcogenides should be regarded as mainly metallic with an ionic contribution [16-20].

2.2 Band structure

Successful calculation of the electron energy spectrum was fulfilled after the accumulation of a considerable amount of experimental data on the band structure of the lead chalcogenides. In particular, it was established that the compounds are narrow-gap semiconductors. The similarities between almost all the properties of the three lead salts indicate that their band structures are also similar. It follows from the similarities in the features of *n*- and *p*- type materials that the edges of the conduction and valence bands

have almost are mirror-image structure, and both the maximum and minimum limiting the energy gap are situated at the same point of the k space. The valence and conduction bands are described by a many-ellipsoid, with the ellipsoids elongated along the <111> directions. The number of the equivalent extrema is four; hence, both the principal extrema are located at the boundary of the Brillouin zone along the <111> directions (L points).

The cubic symmetry of the whole band structure is a consequence of the corresponding lattice symmetry. The presence of the inversion center in the lattice results in at least a double degeneracy of all electron energy bands.

Figure 2.2 shows band structures of PbTe calculated by the psedopotential method [21]. The theoretically calculated values of the energy gaps between levels at special points of the reduced zone, where the combined density of states is maximum, were compared with results of measurements of the ultraviolet spectra [22-23], of electro optical experiments [24,25], and of electron photoemission spectroscopy [26-29].

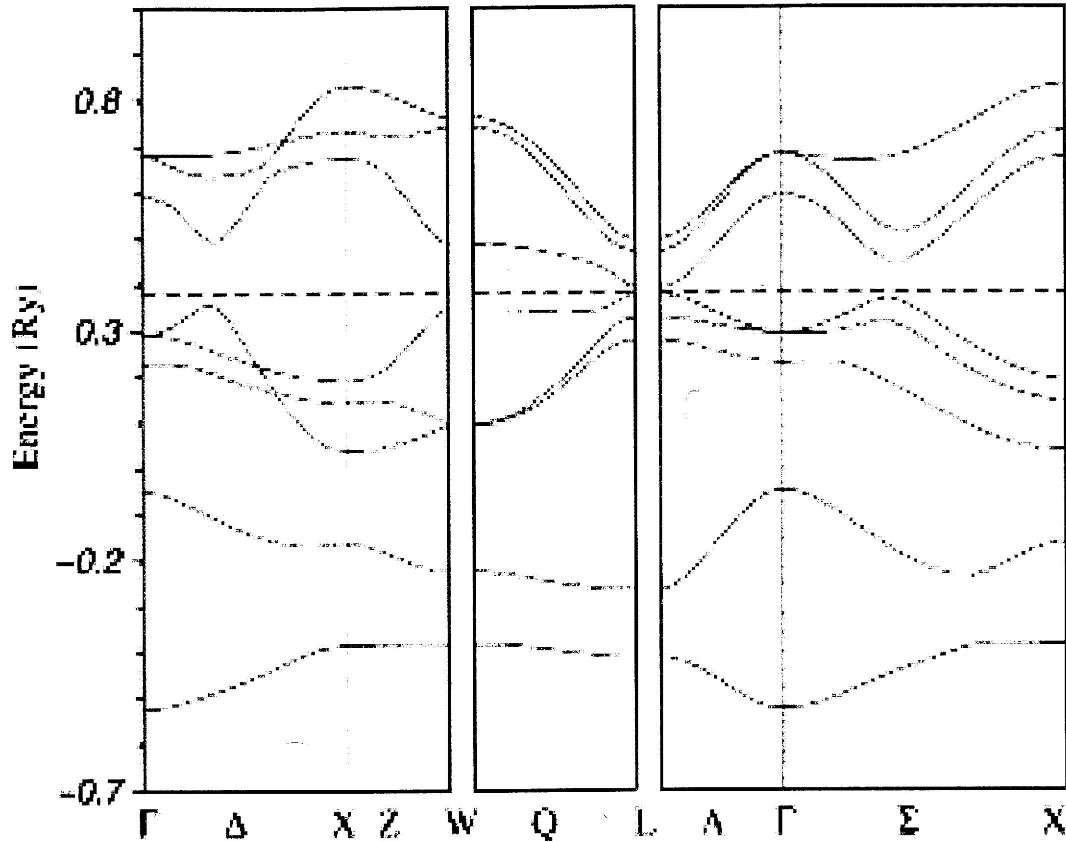

Figure 2.2 Theoretical electronic band structure of PbTe calculated by psedopotential method [21].

The calculations yield a direct fundamental gap at the *L* point of the Brllouin zone. The top of the valence band is described by the even wave function transformed in accordance with the double group representation L^{+}_{6}, and the bottom of the conduction band corresponds to the odd wave function L^{-}_{6}. The wave functions have symmetry of such type the matrix elements of the momentum for states corresponding to the conduction and valence band edges are not equal to zero. This is in accordance with the optical experimental data showing allowed direct transitions at the edge of the fundamental absorption.

The energy gap E_g of lead chalcogenide depends on the temperature, pressure, and

composition of some solid solution. The most important characteristic of any semiconductor, E_g, was experimentally determined in the lead chalcogenides by many optical and transport methods [30-32]. The most precise values of E_g at low temperature were obtained by optical measurements in quantizing magnetic fields [30]. These are given in Tab. 2.2.

Table 2.2 Parameters of the edges of conduction and valence bands in the lead chalcogenides.

Parameter	PbTe	PbSe	PbS
Eg (T=0 K) meV	190	165	286
Eg (T=300K) meV	320	280	410
E_1, meV	171.5	125	263
E_2, meV	12.8	20	20
α, meV/K	0.44	0.506	0.506
θ, K	20	0	0
$\partial E_g / \partial T$, meV/K	0.45	0.51	0.51
$\partial E_g / \partial P, 10^{-3} meV / bar$	-7.5	-9.1	-9.1
m_l	$0.41m_0$	$0.07m_0$	$0.105m_0$
m_t	$0.041m_0$	$0.04m_0$	$0.08m_0$

In contradistinction to the energy gaps of most of semiconductors, the values E_g in the lead chalcogenides increase with an increase in temperature. The relative change of E_g from T=0K to room temperature is not small. In can be characterized by empirical formulas, including

$$E_g(T) = E_1 + [E_2^2 + \alpha^2 (T + \theta)^2]^{1/2} \tag{2.2}$$

With parameters E_1, E_2, α, and θ [4,5] as given in Tab.2.2. In the temperature range from about 50 K up to 400 K, the linear dependence of $E_g(T)$ was obtained, with the

temperature coefficient $\partial E_g / \partial T$ also being given in Tab. 2.2 [4].

The temperature dependence of the energy gap is due to the thermal expansion of a crystal and the interaction of current carriers with phonons. The first component can be estimated if the pressure coefficient $\partial E_g / \partial P$, the compressibility, and the thermal expansion coefficient are known. The measurements of the galvanomagnetic effects have shown [33-35] that the energy gaps in the lead salts decrease under the pressure. The pressure derivatives are given in Tab.2.2. The negative sign of the pressure coefficients means that the lead chalcogenides develop into a gapless state at a high pressure near 20K bar, and such a transformation has been observed [36,37]. As for the two components of the temperature derivative $\partial E_g / \partial T$, estimations [2] have given the result that about half of the temperature-induced gap change can be attributed to thermal expansion and the other half is due to interaction with phonons. Electron effective mass of each material also shown in Tab 2.2.

2.3 Doping

For the IV-VI semiconductors, two alternative methods for adjustment of carrier concentration exist, namely: (1) by control of the crystal stoichiometry, and (2) by doping with various kinds of impurities. The first technique is based on the fact that the IV-VI compounds can accommodate small deviations from the exact 1:1 metal-to-chalcogen stoichiometry by formation of vacancies or interstitials [38]. Since the energy levels of these vacancies are resonant within the conduction or valence bands [39, 40], each Pb vacancy acts as a doubly charged acceptor, and each doping of IV-VI epitaxial layers is to adjust the flux ratio between metal and chalcogen atoms supplied

during growth. This can be most easily achieved by means of a separate chalcogen source. The resulting doping level then depends on the condition of the lead salt source material, on the flux rate from the additional chalcogen source, and on the growth temperature.

For PbTe, the maximum electron concentration achieved in this way is limited to a few times 10^{17} cm^{-3}. For higher excess Pb fluxes, Pb precipitates are formed in the layers, leading to a drastic degradation of the electronic properties [41]. For Te-rich layers, maximum hole concentrations of about 2 x 10^{18} cm^{-3} can be achieved, but very high excess Te flux rates of several monolayers per second are required for this, and the resulting hole concentration strongly depends on the actual growth temperature.

Apart from stoichiometry control, doping can be achieved by various kinds of impurity atoms, ranging from group IIIa (In, Ga, Tl), to group Va (As, Sb, Bi) to group Ib elements (Cu, Ag) [42]. Most of these dopants are amphoteric p- or n-type in character, depending on whether the impurities are incorporated on substitution metal or chalcogen lattice sites [42, 43], which depends on the epitaxial growth conditions. Tl and Bi supplied under chalcogen-rich conditions have proven to be most efficient as dopants and exhibit sufficiently small diffusion coefficients to obtain abrupt doping profiles during MBE growth [44, 45]. Occupying substitutional metal lattice sites, their doping action is readily understood from the fact that the acceptor Tl has one electron less, and the donor Bi one electron more as compared to Pb or Sn. If Bi and Tl are supplied from elemental sources, a high excess chalcogen flux must be supplied during growth in order to ensure complete incorporation at metal lattice sites and to retain a high doping efficiency, in particular, for high doping levels.

A better choice is the supply of Bi and Tl in chalcogenide from [Bi_2Te_3, or Tl_2Te_3 [44]].

Evaporation studies have indicated that Bi_2Te_3 sublimes in the form of mixed BiTe and Te_2 molecules [46, 47]; that is, an excess of Te is always present during growth. Figure 3 shows the result of a Tl doping study by Partin and co-authors [45], indication the measured hole concentration in PbTe layers and the measured Tl flux rate as a function of the Tl_2Te effusion temperature. The linear behavior indicates a near unity doping efficiency up to hole concentration as high as 5 $x10^{19}$ cm^{-3} at a Tl concentration of increased surface defect density. Furthermore, a substantial addition Te flux is required to ensure Tl incorporation at Pb lattice sites even when Tl_2Te_3 is used as the source material [45]. Thallium was found diffuse very slowly in PbTe [43], but for ternary alloy layers its doping efficiency rapidly decreases with increasing energy band gap [48, 49].

The n-type doping in IV-VI semiconductor with Bi_2Te_3 also has been study by several groups [43, 48, and 50]. The Bi concentration was determined by precise calibration of the Bi_2Te_3 flux rate by a quartz crystal microbalance and by extrapolation to lower Bi_2Te_3 effusion temperatures. As is indicated by the dashed line, for Bi concentrations up to 5 x 10^{19} cm^{-3}, each Bi atom contributes one electron to the conduction band. This means that all Bi atoms are incorporated substitution ally at metal lattice sites. In this works, we used the second method for doping PbTe for *n*- or *p*-type source.

References

1. W.W. Scanlon, solid state physics, 9, 83 (1959).

2. Yu.I.Ravich, B.A. Efimova, and I.A.Smirnov, semiconducting lead chalcogenides, ed.L.S.Stilbans (Plenum Press,New York,1970) [Russian original:Nauka,Moscow, 1968].

3. R.Dalven. in solide state physics, ed. H.Ehrenreich, F. Seitz, and D.Turnbull, vol. 28 (Academic Press, New York, 1973), p. 179.

4. G.Nimtz and B.Schlicht, in narrow gap semiconductors, Springer Tracts in Modern Physics, Vol. 98, Springer-Verlag, Berlin, 1983, p.1.

5. Landolt-Burstein, Numerical Data and Functional Relationships in Science and Technology, Gr.III. 17 f, ed. O. Madelung, Springer-Verlag, Berlin, 1983.

6. B.A. Akimov, A. D. Dmitriev, D. R. Khokhlov, and L.I. Ryabova, Phys. Status sol. (a), 137, 9 (1993).

7. A. A. Chudinov, Fiz. Tverd. Tela, 5, 1458 (1963) [Sov. Phys. Solid State,5,1061 (1963)].

8. W. Cochran, R.A. Cowley, G.. Dolling, and M. M. Elcombe, Proc. Roy. Soc. A, 293, 433 (1966).

9. G. Lippman, P. Kaestner, and W. Wanniger, Phys. Status. Sol.(a), 6, K159 (1971).

10. A. J. Miller, G.. A. Saunders, and Y.K.Yogurtcu. J. Phys. C, 14, 1569 (1981).

11. W.E. Tennant, Solid State Commun., 20, 613 (1976).

12. H. B. Callen, Phys.Rev., 76, 1394 (1949).

13. M. H. Cohen, L. M. Falicov, and S. Golin , IBM J. Res. Dev., 8, 215 (1964).

14. P. W. Littlewood, J. Phys. C, 13, 4855 (1980).

15. B. A. Volkov and O. A. Pankratov, Zh. Eksp. Teor. Fiz., 85, 1362(1983).

16. O. E. Kviakovskii and E.G. Maksimov, Usp, Fiz. Nauk, 154, 3 (1988).

17. G. Lucovsky and R. M. White, Phys.Rev. B, 8, 660(1973).

18. R. B. Shalvoy, G.. B. Fisher, and P.Y. Stiles, Phys. Rev. B, 15, 1680 (1977).

19. T. Suski and J. Karpinsk, J. Phys, Chem. Solids, 42, 479 (1981).

20. P. Elders, Phys. Status Sol.(b), 120,735(1983); 121,39 (1984).

21. P. J. Lin and L. Kleinman, Phys. Rev.,142,478 (1966).

22. M. Cardona and D. L. Greenaway, Phys. Rev. A, 133, 1685 (1964).

23. P.J.Lin-chun, J. Phys. Chem. Solids, 31, 2199 (1970).

24. V. V. Sobolev, Phys. Status Sol.(b), 45, K149 (1971).

25. D. E.Aspnes and M. Cardona, Phys. Rev. A, 173,714 (1968).

26. J. Kinoshita and R. Glosser, Phys. Lett. A, 48, 393 (1974).

27. W. E. Spicer and G. J. Lapeyre, Phys. Rev. A, 139, 565 (1965).

28. R. M. Oman and M. J. Priolo, J. Appl. Phys., 36, 2091 (1965).

29. M. Cardona, D. W. Langer, N. J. Shevchik, and J. Tejeda, Phys. Status Sol. (b), 58, 127 (1973).

30. D. L. Mitchell, E. D. Palik, and J. N. Zemel, Proc. 7th international Conference Phys. Semicond., Paris, 1964 (ed. M. Hulin, Dunod, Paris, 1964), Vol. 1, p, 325.

31. H. Preier, Appl. Phys., 20,189 (1979).

32. B. L. Gelmont, T. R. Globus, and A. V. Matveenko, Solid State Commun., 38, 931 (1981).

33. A. A. Averkin, U. V. Ilisavsky, and A. R. Regal, Proc. 6th international conference Phys. Semiconductor Exeter, 1962, published by the Institute of Physics , London (1962), p. 690.

34. W. Paul, M. Demeis, and L. X. Finegold, Proc. 6th international conference Phys.

Semiconductor Exeter, 1962, published by the Institute of Physics , London (1962), p. 712.

35. N. M. Ravindra, Phys. Status Sol. (a) , 52, K151 (1979).

36. P. W. Brydgman, Proc. Amer. Acad. Arts Sci., 76, 55 (1948).

37. N. B. Brandt, O. N. Belousova, V. P. Zlomanov, Ya. G. Ponomarev, and E. P. Skipetrov, Fiz. Tverd. Tela, 19, 437 (1977).

38. T. C. Harman, in physics of IV-VI compounds and alloys, en. S. Rabii (Gordon and Breach, New York, 1974); J. Nonmetals, 1, 179 (1973).

39. G. W. Pratt, Jr., J. Nometals,1, 103 (1973).

40. N. J. Parada, Phys, Rev, B,3, 2042 (1972) ; N. J. Parada and G. W. Pratt, Jr., Phys. Rev. Lett., 22, 180 (1969).

41. G. Springholz, G. Bauer, and G. Ihninger, J. Cryst. Growth, 127, 302 (1993).

42. A. J. Strauss, J. Electron, Mat., 2, 553 (1973).

43. K. Weiser, Phys., Rev. B, 23, 2741 (1981).

44. D. L. Smith and V. Y. Pickardt, J, Electrochem. Soc., 125, 2042 (1978).

45. D. L. Partin, C. M. Thrush, S. J. Simko, and S. W.Gaarenstroom, J. App. Phys., 66, 6115 (1989).

46. J. R. Garcia, A. Boyer, and J. C. Tddenac, Metall., Trans., 22A, 2041 (1991).

47. N.D. Tap, M. Schenk, and P. Schafer, Cryst. Res. Technol., 18,K33 (1983).

48. D.L.Partin, B. M. Clemens, D. E. Swets, and C. M. Thrush, J. Vac. Sci. Technol. B,4,578 (1986).

49. H. Holloway and G. Jesion, Phys. Rev. B, 26,5617 (1982).

50. A. Y. Ueta, G. Springholz, F. Schinagl, and G. Bauer, Thin Solid Films, 306, 320 (1997).

51. Urzhumov. Yaroslav A. " sub-wavelength electromagnetic phenomena in plasmonic and polaritonic nanostructures: from optical magnetism to super-resolution". The report of university of textas at Austin. (2007).

Chapter 3
Growth Technology

3.1 Hot wall epitaxy

Hot wall epitaxy (HWE) is a deposition method developed by Prof.Adolfo Lopez Otero [1] and has proved as a very successful growth method for IV-VI, III-V and II-VI compounds [2-5]. It has been used since the early 1970s for the fabrication of high-quality lead salt layers and multilayer. In contrast to LPE, the layers are grown from the vapor phase under high vacuum conditions. The different source materials are contained and sublimed in the lower part of a quasi closed quartz tube with well-defined temperature gradient along the tube axis. The flux of the sublimed source materials is guided by the hot tube walls to the substrate, which is placed at the end of the tube to condense the epitaxial layer at temperature of 280℃. In this quasi closed system, the consumption of the source material is very small and epitaxial growth occurs near thermodynamic equilibrium. The carrier concentrations of the layers are usually controlled by using an additional chalcogen source zone at the bottom of the tube.

In this work, growth of the *p- and* *n-* type PbTe/PbS multiple mirrors system and PbSe/PbSrSe system have been done by the evaporation of the source materials. All source materials are solids and no additional gas was introduced into the growth chamber. Figure3.1 shows the schematic picture of the HWE growth system. The growth chamber was pumped by turbo molecular pump ULVAC UTM-500 to the ambient vacuum pressure usually about 5 x 10^{-7} Torr. The set of three new substrates was introduced by the load locking system from the loading chamber, which was

pumped separately. Then, their vertical position was lowered to the growth position by mechanically control system.

The growth of VCSEL structure has been done by consist of two hot wall furnaces and which can be moved by stepping motor as shown in Figure 3.1. One hot wall system consists of four source tube. In HW1, *p*-type PbTe, *n*-type PbTe and PbS were used as source for growth of *p*-type and *n*-type multiple mirrors. Bi_2Te_3 was used as donor impurity to get the *n*-type PbTe source. Tl dopant was used as acceptor impurity to get the *p*-type PbTe source. The PbS source was not doped. Te source was used to ensure chalcogen rich during growth. In HW2, PbSe , Bi_2Te_3, Sr, and Se were used as sources for growth of VCSELs active layer. Temperature of the source walls were usually set on 550℃, reservoir set on 300℃, and the substrate temperature was usually 280℃.

The deposition of multiple mirror or superlattice (SL) has been done by constant movement of heated substrate above all source walls. Because all three substrate holders were mounted on the rotating disk, this movement was provided by rotation of this disk. The thickness of each layer in the SL was controlled by time above each wall.

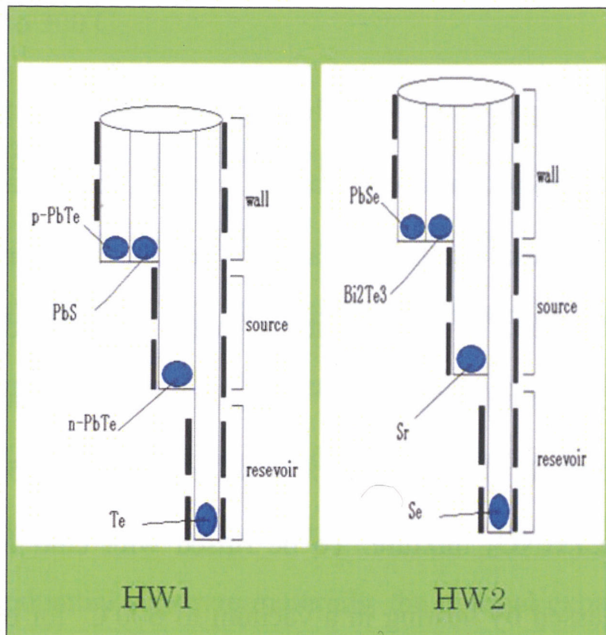

(a) HWE furnaces

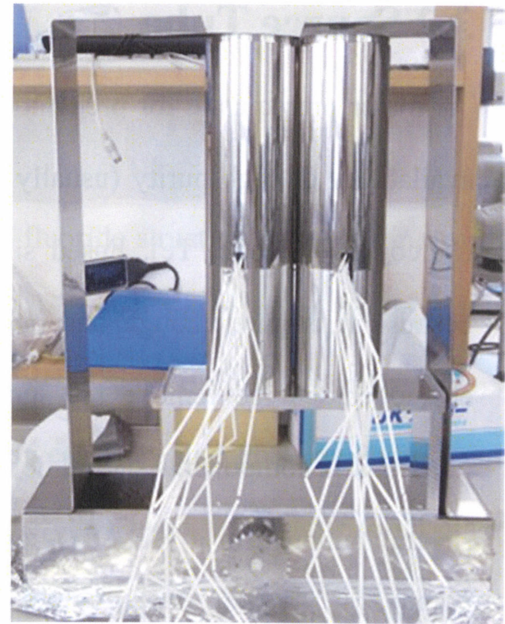

(b) side view

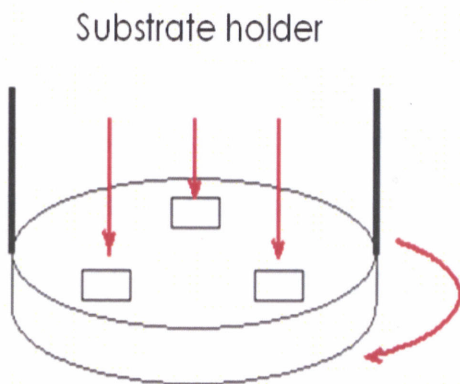

(c) Substrate holder

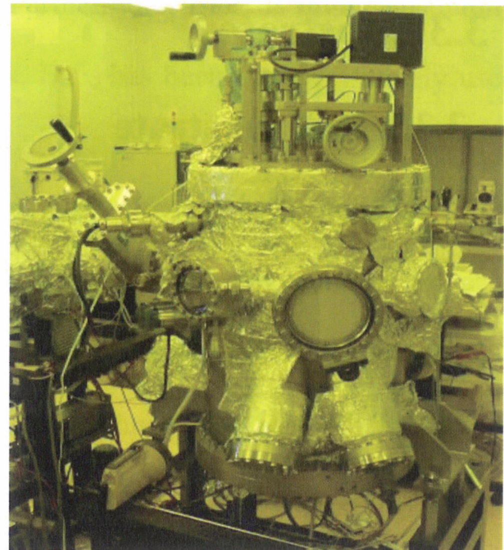

(d) growth chamber

Figure 3.1 Schematic picture of the HWE system for VCSEL, (a) two hot wall furnaces prepared in vacuum chamber: HW1 for *n*- and *p*- type multiple mirror growth, and HW2 for growth of VCSEL active layer. (b) Side view of HWE furnaces. (c) Substrate holder. (d) Growth chamber with background vacuum of 10^{-7} Torr .

3.2 Source Tube

A major prerequisite for preparation of high-quality lead chalcogenide crystals is the availability of high purity (usually 6N grade) containers, starting metals (Pb,Sn), and chalcogens (S , Se, Te). Fused silica (quartz) is used as a main container material because it is pure enough and does not react with the starting materials and metal chalcogenides. To remove the surface contaminations, the ampoules, crucibles, and other quartz components should be thoroughly etched in a 20% solution of HF for 0.5 to several minutes, in a $HF:HNO_3$ or $HCl:HNO_3$ mixture. To be rinsed with cold and boiling deionized water and then out-gassed by heating in a vacuum to 600℃ for one hour.

3.3 Substrates

3.3.1 KCl substrate

In much of the early works, cleaved alkali-halide (NaCl or KCl) single crystal plates served as substrates for the lead chalcogenide epitaxial layer [6,7]. These compounds share the same rock salt crystal structure, have lattice constants not too different from those of the lead salts, and their natural (100) cleavage plane is also the preferred growth direction of the lead salt compounds. However the very large difference in the thermal expansion coefficients between the IV-VI compounds and the alkali halides on the order of $\Delta\alpha = 20 \times 10^{-6} K^{-1}$ results in the formation of micro cracks or even peeling of the epitaxial layers upon thermal cycling. For the alkali halides, KCl is the best compromise, providing a relatively close lattice matching to PbSe ($\Delta a / a = +2.7\%$) as well as PbTe ($\Delta a / a = -2.75\%$), as well as a vapor pressure below 2 x 10^{-6} mbar up

to 300℃.

3.3.2 BaF_2 substrate

Despite their different crystal structure (calcium fluoride structure), the alkaline-earth fluorides (CaF_2, SrF_2, BaF_2), in particular BaF_2, are much better suited for lead salt epitaxy than the alkali halides. This was first demonstrated by Holloway and co-authors [8-10]. On the one hand, the lattice mismatch between BaF_2 and PbSe or PbTe is not very large (-1.2% and +4.2%, respectively). On the other hand, in contrast to all other potential substrate materials, the thermal expansion coefficients are very well matched to that of the lead salt compounds at temperatures greater than 300K. Therefore, the cooling from the epitaxial growth temperature to room temperature or below does not produce significant thermal stains in the layer. Furthermore, BaF_2 is highly insulating and transparent in the mid-infrared region. Thus, BaF_2 has been the most widely used substrate material for the IV-VI epitaxial growth.

References

1. A. Lopez-Otero and L.D. Haas, Thin Solid Films, 1974, 23,1.
2. H. Kinoshita, H. Fujiyasu, A. Ishida and H. Kuwabara, Physics of Narrow Gap Semiconductors (Springer Verlag, Berlin Heidelberg, 1982) Vol 152, pp. 368-372.
3. Y.H. Wu, H, Yang, A. Ishida, H. Fujisasy, S. Nakashima, and K. Tahara, Appl. Phys.Letter, 1989, 54, 239-241.
4. H.Yang, A. Ishida, H. Fujiyasu and H. Kuwabara, J. Appl. Phys. 1989,65 2838-2842.
5. S. Chu, K. Fujimura, D. Suzuki, S. Sakakibara, F. Tanoue, A.Ishida, K, Ishino, K. Aiki,H. Fujiyasu, J. Cryst. Growth, 1998, 189/190, 340.
6. J. N. Zemel, Sol. State Surf. Sci., 1969,1,291.
7. J. N. Zemel, B. D. Jenser, and R. B. Schoolar, Phys. Rev. A, 1965,140,330.
8. H. Holloway, D. K. Hohnke, R.L.Crawley, and E. Wilkes, J. Vac. Sci. Technol., 1970, 7, 586. H. Holloway, E. M. Logothetis, and E. Wilkes, J. Appl. Phys., 1970,41, 3543.
9. H. Holloway, in Physics of thin films, vol.11, eds. G. Hass and M.H.Frankombe, (Academic Press, New York, 1980), p. 116.
10. D. K. Hohnke and S. W. Kaiser, J. Appl. Phys., 1974, 45,892

Chapter 4
Characterization Methods

4.1 Optical property

In this work, to investigate the optical properties of semiconductor films, room temperature optical transmission spectra were measured by Fourier transform infrared (FTIR) spectrometer (Jasco FTIR). The main part of the spectrometer is Michelson interferometer with movable mirror, which inducing a time delay. The beams from the laser source interfere; allow the temporal coherence of the light to be measured at each different time delay setting. By making measuring of the signal at many discrete positions of the moving mirror, the spectrum can be reconstructed using a Fourier transform of the temporal coherence of the light. The detailed of principles of FTIR spectrometer can be found elsewhere [1].

Once the transmittance spectra are measured, their theoretical simulation can be done, using electromagnetic theory of light. When the light beam impacts the multilayered structure, such as semiconductor multilayer mirror, it is partly reflected and partly transmitted, as is schematically show in Fig.4.1.

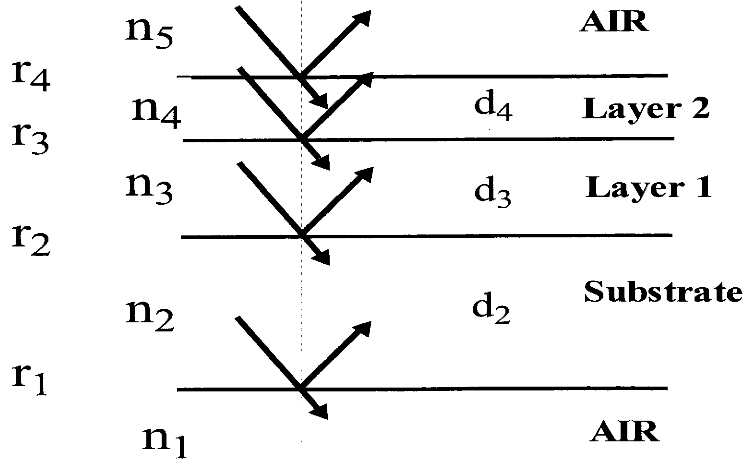

Figure 4.1 Schematic showing reflection and transmission of optical waves inside the multilayered structure.

Normal incident reflection and transmission amplitudes at each interface are given by

$$r_{i+1,i} = \frac{n_{i+1} - n_i - i(K_{i+1} - K_i)}{n_{i+1} + n_i - i(K_{i+1} + K_i)}$$

$$t_{i+1,i} = \frac{2n_{i+1} - 2i(K_{i+1} - K_i)}{n_{i+1} + n_i - i(K_{i+1} + K_i)} \tag{4.1}$$

where n_i is the refractive index of the *i-th* layer and K_i is the extinction coefficient which is given by

$$K_i = \frac{\alpha_i \lambda}{4\pi} \tag{4.2}$$

where α_i is the absorption coefficient of the *i*-th layer, and λ is the wavelength of the incident light. If we consider triple layer reflection and transmission amplitudes taking into account multiple reflections inside *i*-th layer can be written as

$$r_{i+1,i-1} = \frac{r_{i+1,i} + r_{i,i-1} \exp(-2i\phi_i - \alpha d_i)}{1 + r_{i+1,i} r_{i,i-1} \exp(-2i\phi_i - \alpha d_i)} \tag{4.3}$$

while the transmission coefficient is given by

$$t_{i+1,i-1} = \frac{t_{i+1,i} t_{i,i-1} \exp(-i\phi_i - 0.5\alpha d_i)}{1 + r_{i+1,i} r_{i,i-1} \exp(-2i\phi_i - \alpha d_i)} \tag{4.4}$$

and the phase ϕ_i is given by

$$\phi_i = \frac{2\pi}{\lambda} n_i d_i \tag{4.5}$$

where d_i is the thickness of the layer. Thus, transmittance and reflectance are given by $|t_n|^2$ and $|r_n|^2$, respectively.

4.2 X-Ray Diffraction

X-ray diffraction (XRD) is a powerful method to investigate the crystalline structure of various materials. The first XRD patterns of rock salt were obtained in 1971 [2]. Single crystal and powder diffractions were two dominant methods used during first seven decades [3]. Single crystal diffraction method for structural analysis revealed the crystal and molecular structure of inorganic, organic and more recently biological compounds. For semiconductor epilayers, XRD is mainly used to evaluate the quality of the film, determine the mole fraction of alloys, and investigate the thickness, and fine structure of materials with superlattice layers [4, 5].

In 1913, W. L. Bragg observed a diffraction pattern of X-ray radiation after the reflection on crystal structure. He explained this effect by the reflection of X-ray on each atomic plane and their mutual interference. The condition for constructive interference can be written as

$$2D\sin(\theta) = N\lambda \tag{4.6}$$

and is well known as the Bragg law. In the equation , N is the integer representing the order of diffraction, λ is the X-ray wavelength, D is the inter-planar spacing between the atomic diffracting planes, and θ is the angle of incidence. The definition of θ is shown in Figure 4.2.

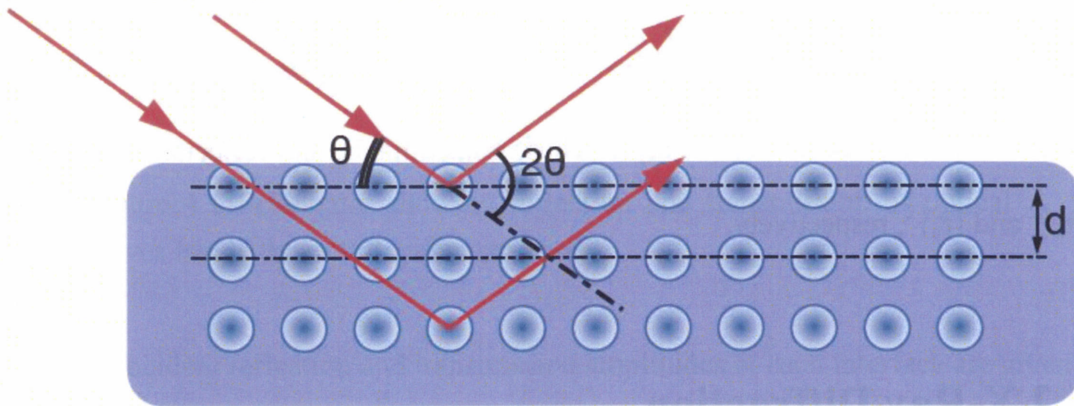

figure 4.2: Bragg diffraction from a cubic crystal lattice and the definition of θ .

In this work, Rigaku RINT Ultima III diffract meter was used to study the crystalline quality, interface abruptness and layer thickness uniformity throughout the superlattice or multiple mirror layers. The typical schematic picture of XRD system is shown in figure 4.3. The X-ray radiation is produced by X-ray tube due to the characteristic X-ray Transitions in a metal anode (this case is Cu) after the interaction between the anode and accelerated high energy electron beam. The wavelength of radiation is in the order of angstroms [Å] (for Cu anode, $K\alpha_1$ is 1.54056 Å and $K\alpha_2$ is 1.54439Å). The beam conditioners are used to collimate and monochromatic the X-rays. The sample is mounted onto the holder which can rotate along three axes: $\omega, \Phi and \Psi$. A scintillation detector is used to collect the diffracted radiation, where the detector can

move through the Bragg angle while scanning. The measured intensity is in counts per second (CPS) units.

There are two basic types of XRD scan modes:

- θ - ω (rocking curve) XRC scan: in this case, the resulting data intensity VS ω (sample angle) show detailed structure of material being investigated. The width of the rocking curve is a direct measure of the range of orientations present in the irradiated area of the crystal, as each sub-grain of the crystal is probed as the crystal is rotated. For a film, which is not exactly epitaxial, the widths of a rocking curve give the information about the quality of the epilayer.
- θ -2 θ XRD scan: the resulting data of intensity vs. 2 θ shows peaks for x-rays satisfying the diffraction condition (4.6). This scan is issued to indentify the lattice constant, and determine the mole fraction of alloys. It is also used to investigate the thickness and fine structure of materials with superlattice layers. While the ideal epitaxial film exhibits only one peak for each diffraction order, ideal superlattice exhibits a set of satellite peaks resulting. The position of satellite peak is also give by the Bragg diffraction condition (4.6), where d in this case means the thickness of one superlattice period. Since any interdiffusion at interfaces between the superalttice layers correlates with the structure of satellite peaks, their sharpness indicate the quality of the interface abruptness and the periodicity of superlattice.

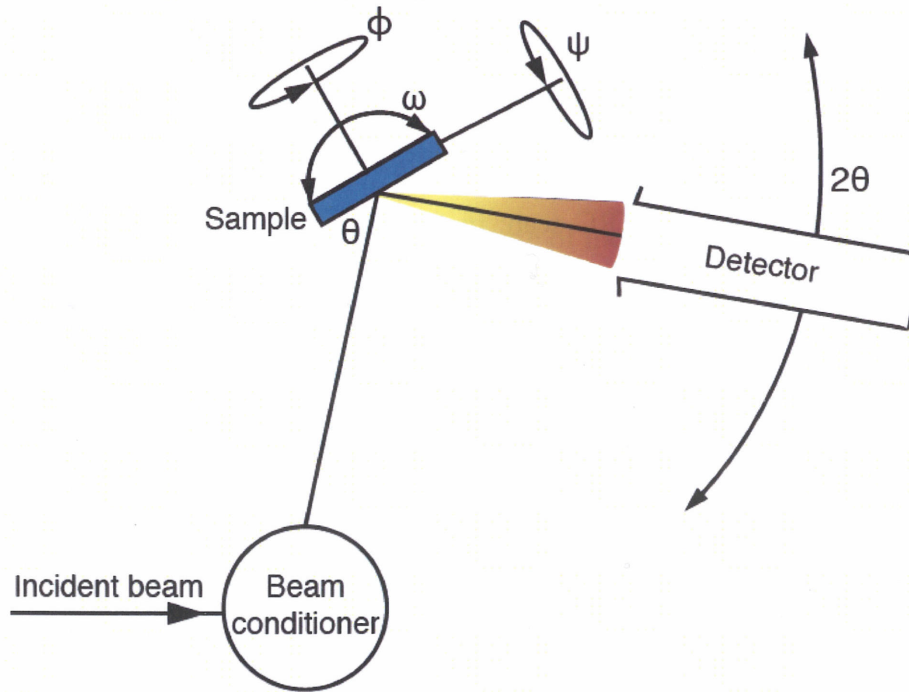

Figure 4.3: Schematic diagram of the XRD setup.

The XRD pattern can be calculated as a summation of reflection intensities for all atomic layers in the structure. The reflection intensity I (θ) can be expressed by

$$I(\theta) = \left| \sum_{mn} f_{mn'}(\theta) e^{i\phi_{mn'}(\theta)} \right|^2 \tag{4.7}$$

and

$$\phi_{mn'} = (4\pi d_{mn} \sin\theta) / \lambda \tag{4.8}$$

Where θ is the incident angle of X-rays, $f_{mn'}$ is the atomic scattering factor of the $mn'-th$ atomic layer ($n'-th$ atomic layer in the $m-th$ superlattice layer) and $\phi_{mn'}$ is the phase difference of X-rays between the first atomic layer in the first superalttice layer and the mn' atomic layer. The value of $\phi_{mn'}$ is calculated using the values θ ,

λ and d_{mn} (the distance between the first and mn' atomic layer). Atomic scattering factor f describes the property of each atom to scatter the X-rays. As a first approximation, these factors are determined assuming that the electron density of each atom is a discrete and spherically symmetric entity. They are independent of the wavelength of radiation and only depend on scattering angle and the type of atom. At zero scattering angles the value for an atomic scattering factor of a given atom has a value equal to the number of electrons in the atom. As the scattering angle is increased, the value of the scattering factor is decreased. The decrease of scattering factor with increasing scattering angle is reasonable because X-ray photons hitting different parts of the electron could of an atom are not expected to scatter in phase with one another. Also, the more diffuse the electron cloud, the more repaid will be reduction in the scattering function with scattering angle.

Owing to the Bragg condition (4.6), the determination of the lattice parameter is possible from the experimental XRD data. This can be used for the monitoring of the stress in ultrathin layers in the superlattice structure. When the lattice parameter d is changed due to the induce stress, the position of XRD peak is shifted. This situation is displayed in Figure (4.4).

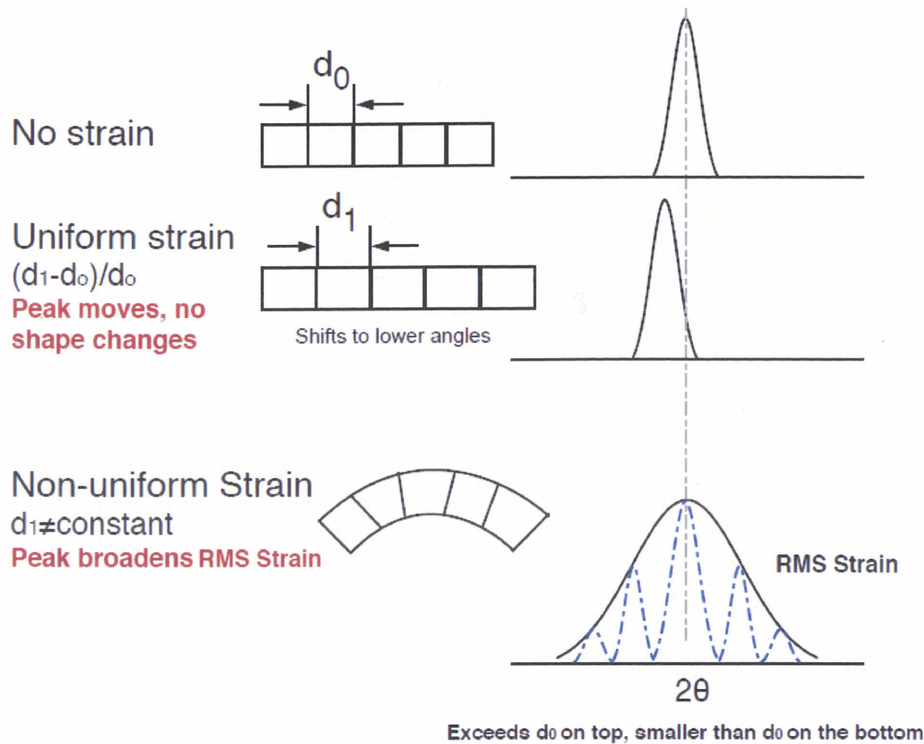

Figure 4. 4 the dependence of XRD peak position and shape on the strain of the film.

4.3 Hall effect measurement

Hall measurements are a standard method for epitaxial semiconductor layers. Some general issues as well as some specific experiments based on the Hall effect are described in this section.

4.3.1 The Hall Effect and the Lorentz Force

When a magnetic field is applied to a conductor carrying a current, an electronic field appears across the conductor in a direction perpendicular to the current and to the magnetic field. This effect was discovered by E. H. Hall in 1879 in thin metallic foils and was named as the Hall Effect. Now it is a very important method for the

investigation of electrical properties of semiconductors.

Figure 4.5 shows a magnetic field $\vec{B}$ applied along the z-axis and an electric field $\vec{E}$ applied along the x-axes. When holes (consider a p-type semiconductor) move in a conducting layer that is introduced in a magnetic field, a Lorentz force $\vec{F}_L$ appears:

$$\vec{F}_L = q\vec{v} \times \vec{B} \tag{4.9}$$

where q is the charge ($q=|e|$, e is elementary charge) and $\vec{v}$ the velocity. If electrodes are placed across the transverse dimension of the layer, a voltage V_H, called the Hall voltage can be measured.

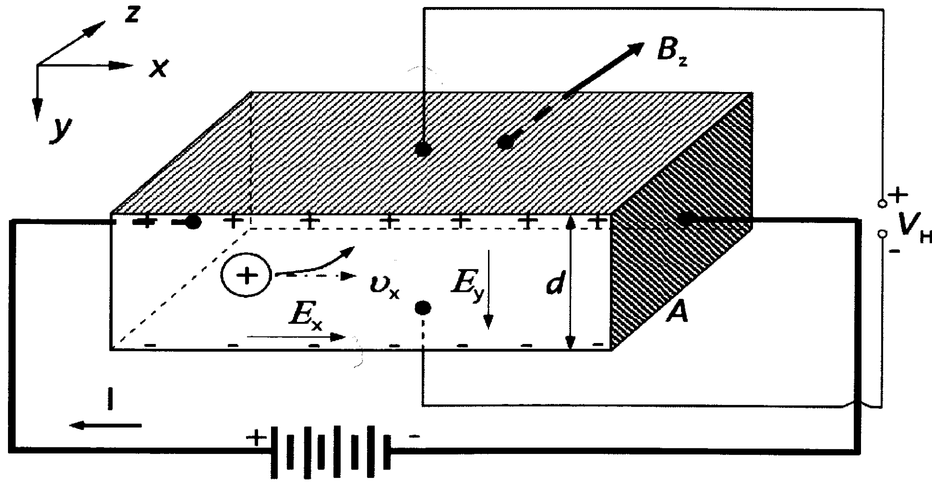

Figure 4.4. Hall Effect measurement setup.

For ideal plate geometry, the Hall voltage can be written

$$V_H = \frac{IB}{qpd} = R_H \frac{IB}{d}, \tag{4.10}$$

where I is the current, B the magnetic field component transverse to the current, p is charge carrier density, d is the thickness of the layer, and

$$R_H = \frac{1}{qp} \tag{4.11}$$

is the Hall coefficient.

A similar result can be obtained for an n-type semiconductor, except that the Hall coefficient is negative:

$$R_H \equiv -\frac{1}{qn}. \tag{4.12}$$

A measurement of the Hall voltage for a known current and magnetic field yields

$$p = \frac{1}{qR_H} = \frac{IB_z d}{qV_H}, \tag{4.13}$$

All the quantities in the right-hand side of the equation can be measured. The majority carrier concentration and carrier type can be obtained directly from the Hall measurement [6].

4.3.2 Van der Pauw method for the Hall measurements

In order to determine both the mobility μ and the sheet density $p_s = p/d$, a combination of a resistivity measurement and a Hall measurement is needed. The van der Pauw technique is widely used in semiconductor analysis for this purpose [7]. The sample of thickness d may have any shape, and have to satisfy:

- The contacts are at the circumference of the sample
- The contacts are sufficiently small
- The sample is homogeneous in thickness and composition

• The surface of the sample is singly connected, i.e., the sample does not have isolated holes.

The objective of the resistivity measurement is to determine the sheet resistance R_s. There are two characteristic resistances R_1 and R_2, associated with the contacts shown in Fig. 4.6. R_1 and R_2 are related to the sheet resistance R_s through the van der Pauw equation

$$\exp(-\frac{\pi R_1}{R_s}) + \exp(-\frac{\pi R_2}{R_s}) = 1$$
$$R_1 = \frac{V_{DC}}{I_{AB}}, R_2 = \frac{V_{BC}}{I_{AD}}, R_s = \frac{\rho}{d}, \tag{4.14}$$

where ρ is the electrical resistivity. This equation can be solved numerically for R_s.

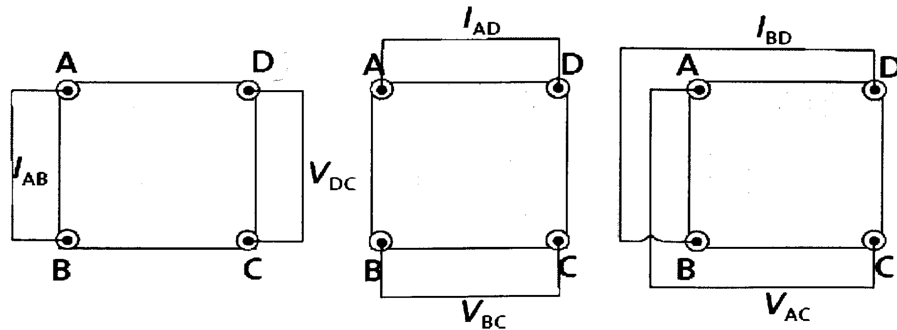

Figure 4.6 A schematic square van der Pauw configuration.

The objective of the Hall measurement in the van der Pauw technique is to determine the sheet carrier density p_s by measuring the Hall voltage V_H. To measure the Hall voltage V_H, a current I is forced through the opposing pair of contacts B and D and the Hall voltage V_H (=V_{AC}) is measured across the remaining pair of contacts A and C with

and without the magnetic field B (in Fig. 4.5 magnetic field is perpendicular to the page plane). Once the Hall voltage V_H is established, the resistance R_3 can be calculated via

$$\Delta R_3 = \frac{\Delta V_{AC}}{I_{BD}} = \frac{R_H B}{d}, \tag{4.15}$$

where $\Delta V_{AC}=V_{AC}$(measured voltage between A and C with magnetic field)-V_{AC}(without magnetic field).

For the carrier density it can be written

$$p = \frac{1}{R_H q} \tag{4.16}$$

and in the case of highly doped semiconductors

$$\rho = \frac{1}{qp\mu_H}. \tag{4.17}$$

The Hall mobility μ_H can be found as

$$\mu_H = \frac{1}{qp\rho} = \frac{R_H}{\rho}. \tag{4.18}$$

R_H and ρ can be found from the four resistance measurements

$$R_H = \frac{d\Delta R_3}{B}, \tag{4.19}$$

$$\rho = \frac{\pi d}{\ln 2}\frac{R_1 + R_2}{2} f_{vdP}, \tag{4.20}$$

where f_{vdP} is a correction factor which depends on contact symmetry. For a square sample $f_{vdP} = 1$.

References

1. B.C. Smith, Fundamentals of Fourier Transform Infrared Spectroscopy (CRC, 1995).
2. D. Bowen and B.K.Tanner, High Resolution X-ray Diffractometry And Topography (taylor and Francis, 1998).
3. B.E. Warren, X-ray Diffraction (Addison- Wesley, 1969).
4. M. E. Vickers et al., Journal of Appl. Phys., 2003, 94,1565.
5. S. A. Stepanov et al., Phys. Rev. B, 1998, 57,4829.
6. S.M. Sze, Semiconductor devices, Physics and technology, 2nd ed., John Wiley & Sons, New York, 2001, pp. 564.
7. L. J. van der Pauw, A method of measuring specific resistivity and hall effect of discs of arbitrary shape, Philips Research Reports, 1958, 13, p-9.

Chapter 5 Design and Fabrication of Electrically Pumped VCSEL

5.1 Introduction

In recent photonics research fields, the vertical cavity surface emitting lasers (VCSELs) have become one of the hot topics. The unique geometry of VCSELs results in several significant advantages over their edge emitting counterparts, including a low threshold current, single- longitudinal-mode operation, circular output-beam profile. These advantages make VCSELs promising as compact light source for future applications in optical communications, interconnects, optical storage and as pump source [1-4].

In general, VCSELs consists of an active region sandwiched between two distributed Bragg reflectors (DBRs) [5]. The thickness of the active region is only several hundreds of angstrom, when the resonator length is only in wavelength order in VCSELs. It is difficult to obtain enough gain in such thin active region. Therefore, mirrors with high reflectivity are necessary in VCSELs in order to reduce the loss of the resonant cavity and achieve stimulated emission [6, 7]. For these mirrors, typically a multilayer stack consisting of quarter-wavelength dielectric or semiconductor layers with low- and high-index materials are used. The DBRs, which constitute a sophisticated Fabry-Perot resonator in VCSELs, provide more than 99% reflectivity. However, the DBRs would reduce the output power seriously as the increased resistance when the reflectivity becomes higher and higher [8, 9]. This phenomenon, which is caused by self-heating, is particularly evident in the *p*-type DBR [10]. Self-heating, which increases the temperature of the cavity and changes the refractive index and the band gap of each semiconductor layer, will reduce the output power.

Lead salt mid infrared optical pumped VCSELs were first demonstrated by Springholz group [33, 34], and in the same year 2000, Shi group published for

wavelength between 4.5 and 6μm [35]. Within a short time, the performance of optically pumped lead salt VCSELs was drastically improved with pulse laser emission now reaching up to 65℃ [36]. In addition, Springholz group have achieved CW emission at long wavelength up to 8μm [37], which represent the longest wavelengths of all VCSELs up to now. In this chapter, we design and fabricate the new VCSELs structure based on lead salt for electrical pumped laser.

5.2 Theory of VCSEL

The first all-semiconductor VCSELs were demonstrated in 1989 by Jewell *et al.* using epitaxial Bragg mirrors [11]. As shown schematically in Figure 5.1, these lasers have a completely different design as compared to edge emitters because the resonator axis is perpendicular to the growth plane of the layers. The Fabry-Perot cavity is formed by two high reflectivity interference mirrors consisting of a stack of dielectric layers. Thus, the generated radiation is reflected and amplified many times across the active cavity region until it is coupled outward vertically through the top or bottom mirrors. Generally, the resonator length of VCSELs is comparable to the optical emission wavelength. This is because pumping can occur only over a limited thickness of the active region and because in this way single mode operation is easily obtained. On the other hand, to compensate the short length of the gain medium, the reflectivity of the VCSEL mirrors must be very high at about 99% as compared to typically only 30% for edge emitters. Due to the rapid progress in research and development [12-14], already in the middle of 90th VCSELs have become available on a commercial basis [15]. Up to now, however, most work has been focused on III-V electrically pumped VCSELs with emission from the visible to NIR spectral region (400 nm [16, 17] to 1.5 μm [18, 19]). Owing to the tremendous difficulties in fabrication of high reflectivity infrared Bragg mirrors.

A particular feature of micro cavity lasers is the large mode spacing of their resonator structure. For a dispersion free dielectric medium, the separation $\triangle k_{mode}$ of these Fabry-Perot modes is constant in wave number of frequency space and is given by

$$\Delta k = (2nL_{cav})^{-1} \tag{5.1}$$

Where L_{cav} is the cavity length, which in a surface emitting laser is the total layer thickness of the cavity region, and n is its refractive index. As the cavity length is comparable to the emission wavelength of the active medium, the laser emits on one of the first fundamental cavity modes k_m , which are given by

$$\begin{aligned} k_m &= m(2nL_{cav})^{-1} \\ \lambda_m &= (2nL_{cav})/m \end{aligned} \tag{5.2}$$

Where the integer number m = 1,2,3 … corresponds to the order of the mode. Thus, first order emission occurs for a microcavity laser with $L_{cav}=\lambda/2$, and for VCSELs usually the cavity length is typically in the range of $\lambda/2$ to 2λ .

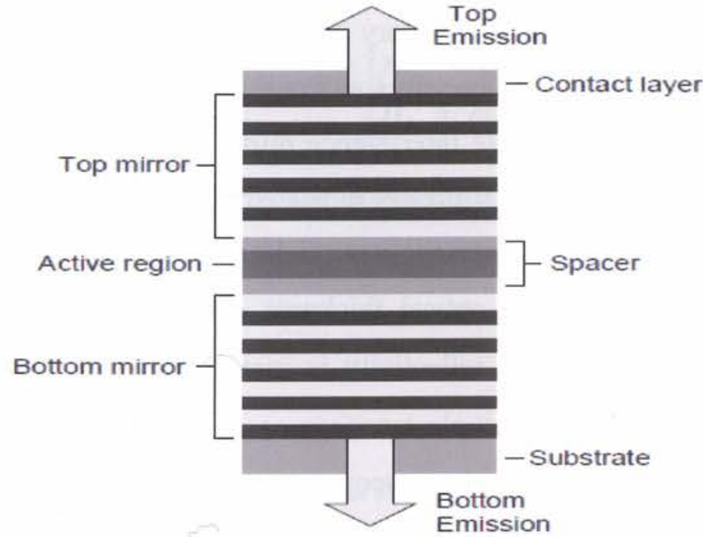

Figure 5.1 Schematic representation of a VCSEL, consisting of two high reflectivity Bragg mirrors of multiple $\lambda/4$ layer pairs with alternating high and low refractive index and an active region inserted between. The laser light is emitted in the vertical direction through the top or bottom Bragg mirror.

An important parameter that characterizes the quality of the resonator is the finesse or quality factor F of the cavity given by

$$F = \pi \frac{\sqrt{R}}{1-R} = \frac{1}{m}\frac{k_m}{\delta k_m} \tag{5.3}$$

Where R is the reflectivity of the mirrors at the resonance wavelength. The finesse describes how often the photons pass back and forth through the gain region before being emitting. Thus, the higher the finesse, the lower the threshold of the laser. As indicated by equation (5.3), the finesse can be easily determined by measuring the width of the cavity resonance peak δk_m in transmission or reflectivity spectra. Typical finesse values required for VCSELs are around 300, which corresponds to mirror reflectivity of about R= 99%. Due to the large mode spacing of VCSELs, the gain spectrum of the active medium overlaps only with one resonator cavity mode. Thus, lasing occur only on a single mode. Other advantages including simplified planar

processing and monolithic integration in arrays and logic or control devices, and their symmetric circular output beams with very small beam divergence angles allow an easy coupling into optical fibers. Finally, very low threshold currents can be obtained.

High reflectivity epitaxial Bragg interference mirrors are crucial elements of vertical cavity surface emitting lasers. As already indicated in Figure 5.1, these mirrors consist of multilayer stacks of optically transparent dielectric layers with alternation low and high refractive indices and an optical thickness equal to one quarter of the target wavelength λ_T for which the reflectivity is maximized. The reflectivity of Bragg mirrors is purely caused by multiple interference effects and can be tuned arbitrarily from 0 to 100% by changing the layer sequence or number of layer pairs. In addition, Bragg mirrors exhibit very small intrinsic absorption unlike metallic mirrors, where the high reflectivity is due to extinction of light. Therefore, Bragg mirrors are particularly well suited for application such as VCSELs where very high reflectivities without any losses are required.

For an ideal Bragg interference mirror consisting of N periods of dielectric $\lambda/4$ layer pairs of alternating low and high refractive indices n_1 and n_2, at the target wavelength λ_T all waves reflected at the interfaces are exactly in phase. Thus, the reflectivity is high and at this wavelength is given by

$$R(\lambda_T) = \left[\frac{1 - n_f / n_i (n_1 / n_2)^{2N}}{1 + n_f / n_i (n_1 / n_2)^{2N}} \right]^2 \qquad (5.4)$$

Where n_i and n_f are the refractive indices of the media in front and behind the mirror. n_1 and n_2 are the refractive indices of the mirror material, respectively. Equation 5.4 shows that the reflectivity is essentially determined only by two parameters, namely, the total number N of $\lambda/4$ layer pairs and the refractive index ratio or refractive index contrast $\Delta n / \bar{n} = 2|n_2 - n_1| / |n_2 + n_1|$. Obviously, the condition that all reflected waves are in phase is fulfilled exactly only for the target wavelength. Therefore, with increasing deviation from this wavelength, the Bragg mirror becomes less ideal and the reflectivity remains high such that a high reflectivity spectral region called stop band is formed. The whole reflectivity spectrum of such a mirror can be calculated using the transfer matrix method [20, 21]. The result shows that the relative width of the stop

band $\Delta k_{stop} / K_T$ depend only on the refractive index contrast [22]

$$\frac{\Delta k_{stop}}{\Delta k_T} = \frac{4}{\pi} \arcsin \left| \frac{n_1 - n_2}{n_1 + n_2} \right| \tag{5.5}$$

Thus, the stop band is wide only for Bragg mirrors with very high refractive index contrast and outside of this region the reflectivity rapidly falls off.

5.3 Mirror materials

For high reflectivity Bragg mirrors, several requirements must be fulfilled:

(1) The achievement of smooth $\lambda/4$ layer interfaces to avoid diffuse light scattering.

(2) A precise control of the layer thickness to obtain the desired target wavelength.

(3) The use of a sufficient number N of high refractive index contrast layers.

(4) For laser applications, the mirror materials should exhibit a high thermal conductivity for efficient heat dissipation.

(5) For electrical pumping, the materials must also have a good electrical conductivity, low resistance.

(6) For monolithic integration in a vertical laser device, the mirrors must be grown epitaxially onto the substrate and should be compatible with the growth of the active region. All layers should be reasonable lattice matched to prevent defect formation.

Many groups use the lead salt compounds two type of dielectric materials are well suited as low refractive index layer, these are the wide gap Eu-chalcogenide semiconductors EuSe and the insulator BaF_2 with a band gap in the UV range, electrical conductivity of these materials are very low, and don't suit for electrical pumped VCSEl structure. In this work, we use PbTe and PbS as mirror materials. The two materials satisfy all the properties described above.

5.4 Preparation of PbTe and PbS films

PbTe and PbS films were grown to measure the growth properties using HWE system

as shown in chapter 3. The sample was grown on BaF_2 (111) substrate. Bi_2Te_3 (200ppm) was added in PbTe source as donor impurity for prepare n-type PbTe. Tl_2Te_3 (200ppm) was added as acceptor impurity for p-type PbTe source. The source temperatures of *n*-type PbTe, *p*-type PbTe and PbS source were 550℃, and temperature of Te source was 300℃. During the growth , the substrate temperature was set at 280℃. The growth rates and electrical properties are shown in Tab 5.1. Carrier concentration of *p*-type PbTe film was 4.9 x 10^{18} cm^{-3}, and that of *n*-type PbTe was 8.6 x10^{17} cm^{-3}. The carrier concentration of nondoped PbS film was 2.6 x 10^{18} cm^{-3} with *p* type condition. This condition is suitable to make low carrier concentration high reflectivity Bragg mirrors. Optical transmittance measured by FTIR are shown in Figure5.2. The blue dashed line shows theoretical absorption coefficient of each film. During the theoretical calculation, we also considered the free carrier absorption in each film, and the free carrier absorption did not affect seriously the reflectivity in the resonant region of the VCSEL. The thickness of the each film was calculated from optical transmittance spectrum.

Table 5.1 Electrical properties of PbTe and PbS and growth rate.

Name	growth time (s)	thickness (μm)	Hall measurement data				growth rate (Å/s)
			Resistivity (Ω-cm)	Mobility (cm2/V-s)	P/N	carrier concentration (/cm3)	
p-PbTe	1800	2.1	0.0017	770	p	4.9E+18	11
n-PbTe	1800	4.1	0.0049	1500	n	8.6E+17	22
PbS	1800	1.3	0.091	270	p	2.6E+17	7

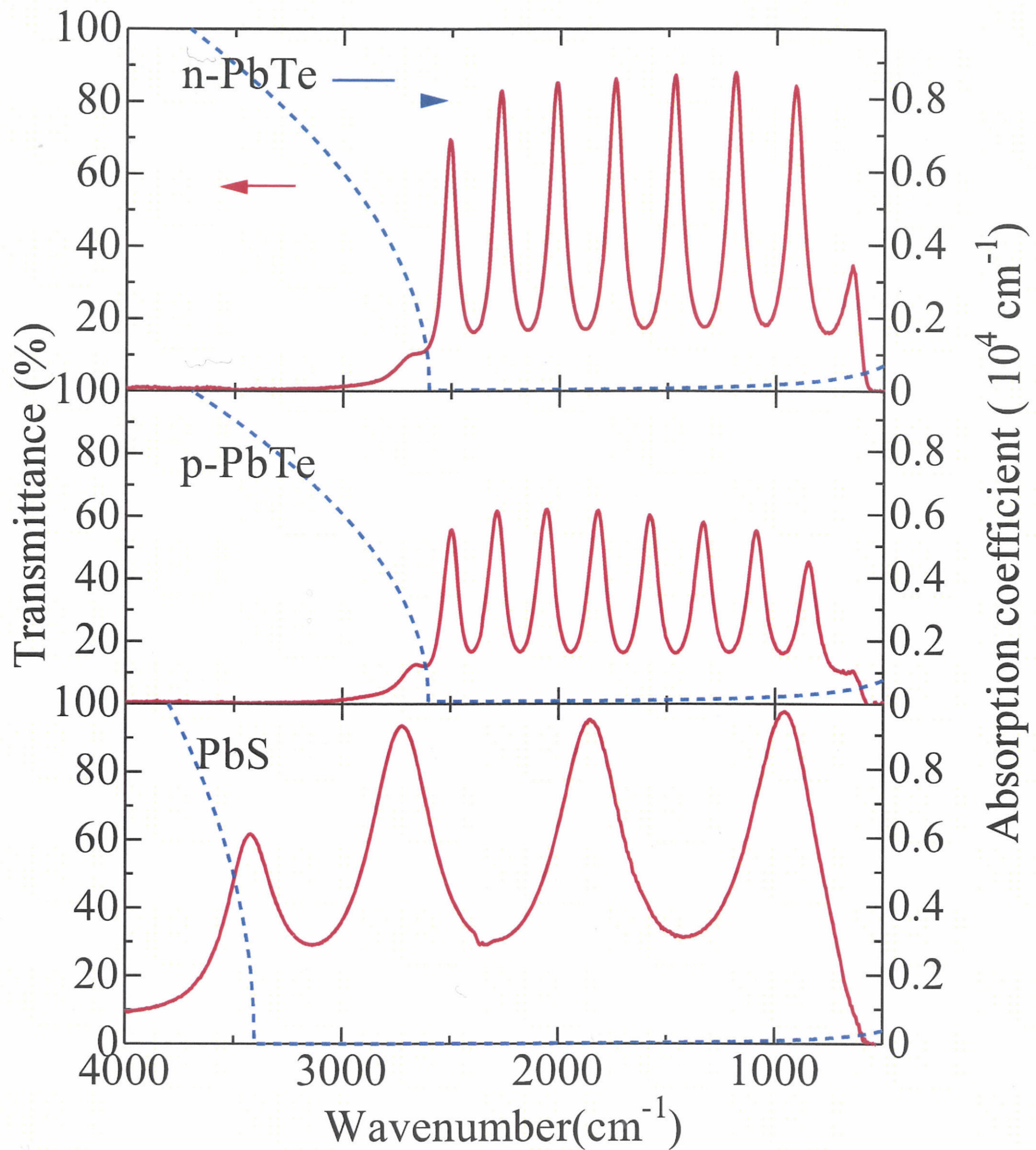

Figure5.2 Optical transmission spectra of PbTe and PbS films at 300K. Blue dashed lines shows calculated absorption coefficients of the films.

5.5 PbTe/PbS multiple mirror

The mirrors employed in a VCSELs are stacks of many pairs of layers, and the thickness of each layer is $\lambda/4n$ (n is refractive index of material) at the design

wavelength λ. Each pair is composed of a high and low refractive index layer. Although the reflectance at each interface is small, all the reflective amplitudes add in phase and the net reflectivity calculated by the amplitude squared can be above 99%. The refractive indexes of PbTe and PbS are 5.6 and 4.0, respectively, and six or seven periods of PbTe/PbS multiple layers are enough to obtain a reflectivity exceeding 99%. Table 5.2 shows the electrical properties of PbTe/PbS multiple mirrors. The *p*-type multiple mirrors for 6 μm VCSEL structure is designed with p-type PbTe and non-dope PbS, which is consist of seven layers PbTe and six layers PbS as shown in figure 5.3. The carrier concentration was about 1.4 x 10^{18} cm^{-3}. The same structure of n-type Bragg mirror was designed with n-type PbTe and non-dope PbS, and the carrier concentration was about 3.5 x 10^{17} cm^{-3}.

Table5.2 Electrical properties of PbTe/PbS multiple mirrors

Sample Name	substrate	Hall measurement data			
		Resistivity (Ω-cm)	Mobility (cm^2/V-s)	P/N	carrier concentration (cm^{-3})
mirror021	BaF_2	0.0065	670	p	1.4E+18
mirror022	BaF_2	0.019	910	n	3.5E+17

Figure 5.4 shows the room temperature transmission spectra of *p*-, and *n*-PbTe/PbS multiple mirrors (red line) measured by FTIR, and the theoretical transmission spectrum of samples fitted to experimental data (dashed line is transmittance, blue line is reflectance). The reflectivity of multiple

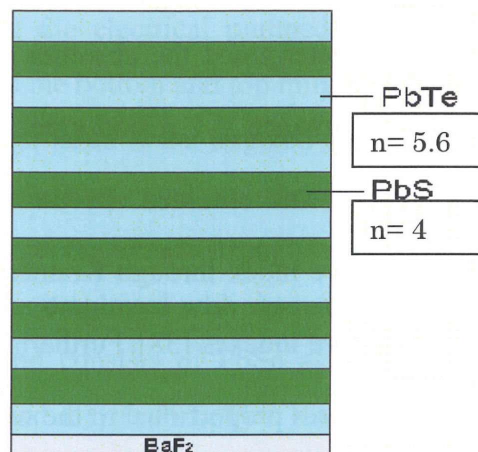

Figure 5.3 Schematic of multiple mirror structure. The mirror consists of seven layers PbTe and six layers PbS.

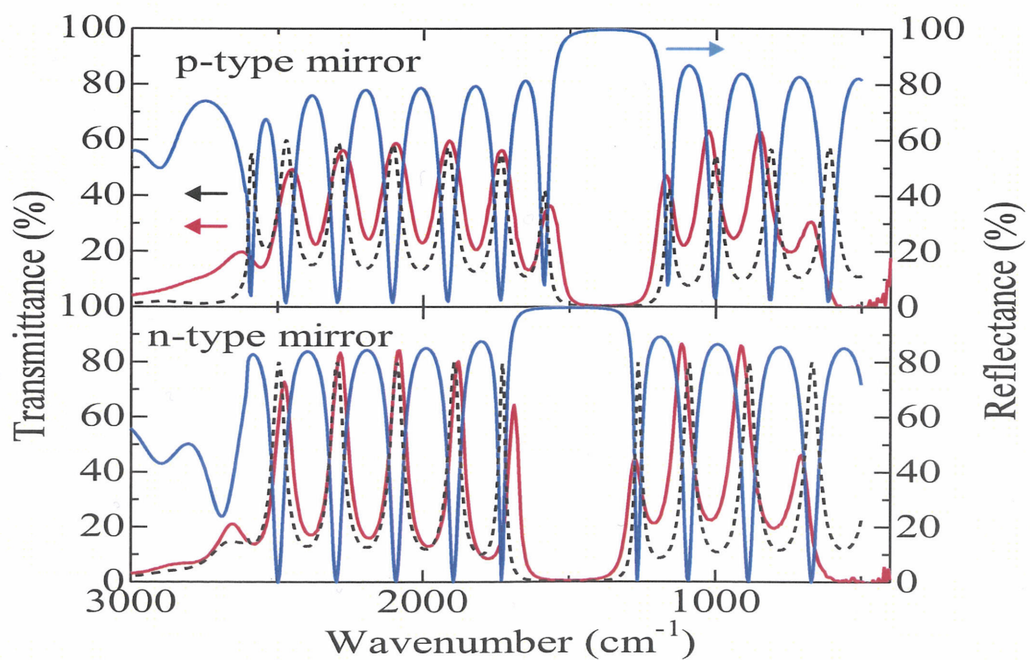

Figure 5.4 : Room temperature transmission spectra of PbTe/PbS multiple mirrors (red line) measured by FTIR and its theoretical calculation (dashed line), blue line shows theoretical reflectance. The reflectivities of p- and n- type mirrors are 99.2%, 99.3%, respectively.

mirrors are more than 99%. We determined the absolute reflectance considering that reflectance + transmittance + absorbance = 1. Good agreement between experimental and theoretical reflection spectra was obtained. In the theoretical calculation, we considered a dispersion of refractive index through Kramers-Kronig relations between absorption coefficients and refractive indexes [38]. Furthermore, we also considered the free carrier absorption which increases proportional to the wavelength squared, to fit the theoretical spectra to experimental ones. The absorption coefficient 170 cm^{-1} at the central wave number of the mirror gives theoretical reflectance of 99.2%, absorbance of 0.3%, and transmittance of 0.5%. Thus the free carrier absorption existing in the conductive multiple mirrors does not strongly affect the reflectance in this carrier concentration. So this conditions of electrical properties of *n*-, and *p*- multiple mirrors are suitable for electrically pumped VCSEL.

5.6 VCSEL structure

For the design of the electrically pumping IV-VI semiconductor VCSEL structures, several parameters must be optimized. First, the vertical resonator structure must have a high finesse in order to obtain low laser thresholds. This can be achieved using Bragg mirrors with high refractive index contrast (eg. PbTe and PbS). Second, the active region should have high infrared luminescence efficiency. For this purpose, both lead salt quantum well structure and bulk like binary epitaxy layers can be as well as single lead salts layer [23]. To adjust the emission wavelengths, ternary alloy of the lead salts with Eu, Sr or Sn chalconenide compounds can be used, this tunes the energy band gap can be turned over a wide range from below hundred to several hundreds of meV [24-30]. The third design issue is the matching of the cavity resonance mode to the emission of the active region. This is crucial because, in contrast to edge emitting laser, the mode spacing of VCSELs is generally much wider than the width of the gain

spectrum and because lasing can occur only if the active region emits into a resonator mode. Finally, to realize the electrical pumped VCSELs with ready to use at low threshold current, it needs the bottom and top mirrors have good electrical conductivity.

Another essential design issue is the targeted operation temperature of the VCSELs because the optical constants as well as the energy band gaps and luminescence wavelengths of the lead salt compounds strongly vary with temperature.

A VCSEL structure was employed wtih resonant design intended for liquid nitrogen temperature operation, and consists of PbSe as the active layer between the p-type PbTe/PbS Bragg mirror and n-type PbTe/PbS Bragg mirror. PbSe exhibits a still lower Auger coefficient compared to PbTe which should lead to lower threshold current. In the resonant design, the active layer has a thickness of a multiple $\lambda / 2$ of the design wavelength λ. Prior to the growth of laser structure, we investigated optical and electrical properties of non doped PbSe film. Figure 5.5 shows PbSe transmission spectra depending on temperature. Red line shows the data measured by FTIR at room temperature. The absorption edge is about 2200 cm^{-1}, and band gap is 280 meV. During the sample cooling by liquid nitrogen, the absorption edge shifted to longer wavelength. The absorption edge at 90K was 1450 cm^{-1}, which corresponds 179 meV in energy. From this result, the emitting wavelength for the PbSe active layer is less than 7μm for the temperature above 90K. The Tab. 5.3 shows electrical property of non doped PbSe. Carrier concentration was 2.7×10^{17} cm^{-3} (*p* type). Growth rate was 5Å/s for the PbSe source temperature 520℃. These film properties are suitable as the active layer of the VCSEL.

Table 5.3 Electrical properties of non doped PbSe film.

Sample name	Mobility (cm^2/Vs)	Carrier Concentration (cm^{-3})	Thickness (μm)	Growth rate (Å/s)
PbSe004	330	2.7E+17 (p)	7.3	5

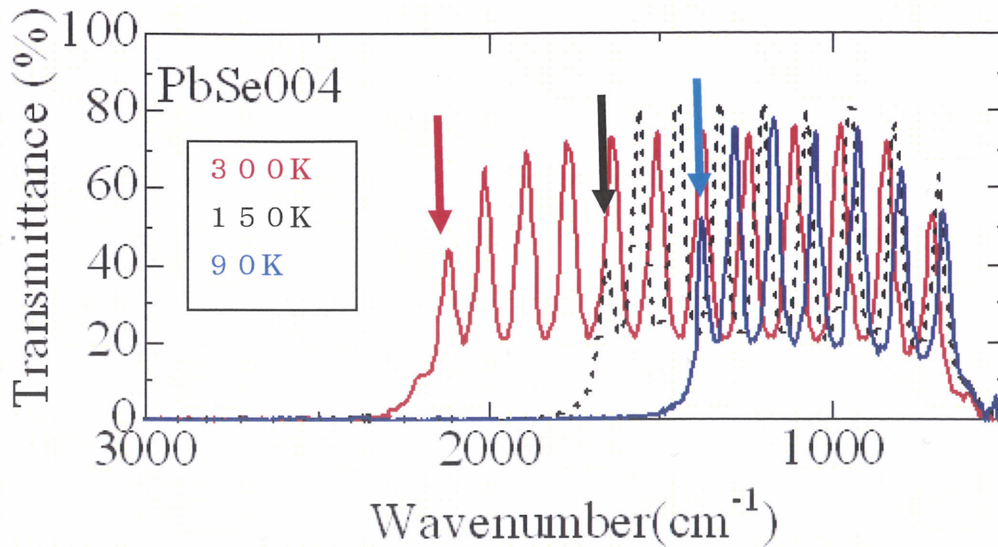

Figure 5.5 Transmission spectra at 300K, 150K and 90K for non doped PbSe. Absorption edge shift to low wavenumber side with decreasing temperature. Absorption edges are shown by arrows, owing to positive temperature dependence of the band gap.

The resonant wavelength of the VCSEL was designed about 6μm suitable for the operation around 150K. Because no cleavage is required for fabrication of VCSEL, lead salt VCSELs can be grown on readily available substrates such as BaF_2 (111) , whereas high cost single crystalline lead salt substrates are needed for conventional diode lasers. Many works have proven BaF_2 to be an excellent substrate material for lead salt heterostructures and multilayer. It is not only readily available in high crystalline quality, but is also optically transparent and offers a five times larger thermal conductivity compared to lead salt substrate. This allows a much better heat dissipation during the laser operation. Also, BaF_2 has a much higher mechanical hardness, which facilitates the processing of the laser structures. As a consequence, up to now lead salt VCSELs have been grown on BaF_2 substrates. On the other hand, BaF_2 exhibits (111) natural cleavage planes as opposed to the preferred (100) planes for the lead salt compounds.

The cavity was formed between the bottom Bragg mirror and the top Bragg mirror as shown in Figure 5.6. The thickness of PbSe was $\lambda/2n$ (n=5) about 0.6 μm. The bottom mirror is p-type, the thickness of PbTe (0.27μm) and PbS (0.38μm) was decide by $\lambda/4n$ (n is refractive index, n_{PbTe}=5.6, n_{PbS}=4). The top mirror was n-type. The FTIR transmission spectrum of the cavity structure at 300k is shown in Figure 5.7, illustrating

this high optical quality of the cavity structure. Within the wide stop band region, a sharp cavity resonance peak was observed. The red line shows experimental transmission spectrum. The dotted line shows theoretical one, and blue solid line shows theoretical reflection spectrum, then we can get the reflectance spectrum. The reflectivity of Bragg mirror is more than 99%.

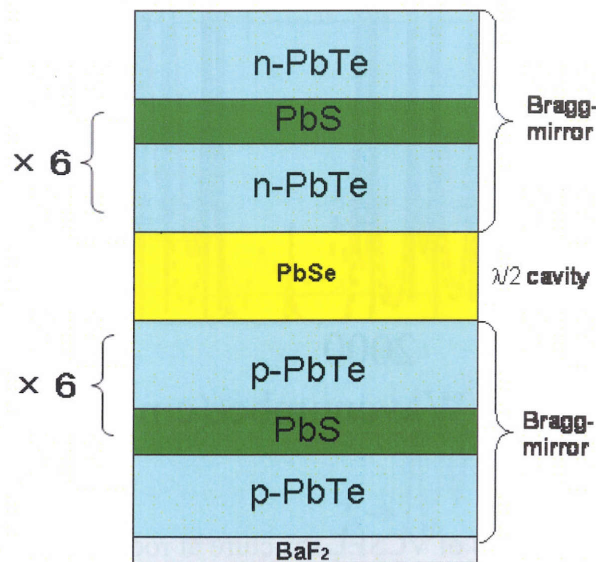

Figure 5.6 Schematic of electrically pumped VCSEL structure.

We also measured temperature dependence of transmission spectrum as shown in Figure 5.8. As the temperature is lowered, the resonance absorption edge shifted to longer wavelength, and the resonance peak was damping due to interband absorption at PbSe band gap depending on temperature. The blue dashed line shows calculated absorbance in active layer.

The micro cavity structure can be also used as a sensitive detector for determining the dispersion of the active region absorption. Because the width of the cavity resonance peak is linearly related to the cavity absorption [32]. The more detail, we will introduce in next chapter.

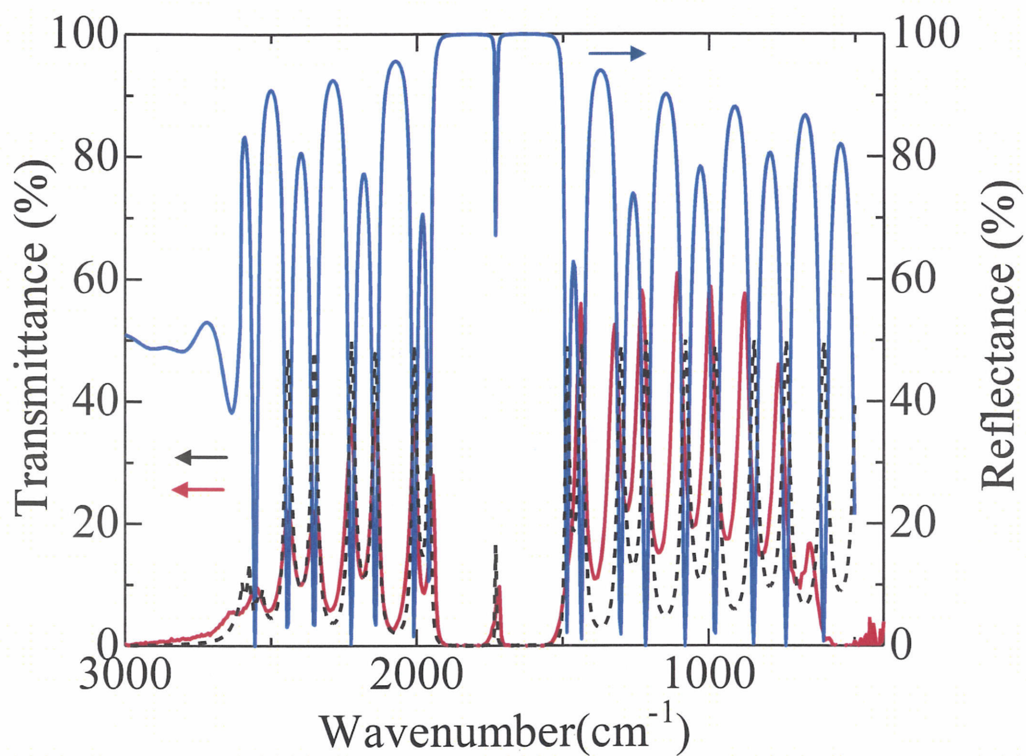

Figure 5.7 Optical properties of VCSEL structure at room temperature, red line shows the experimental data measured by FTIR, while dashed line and blue line describes the theoretically calculated transmission and reflection spectra, respectively. The reflectivity of Bragg mirror is more than 99%, and resonant peak is observed.

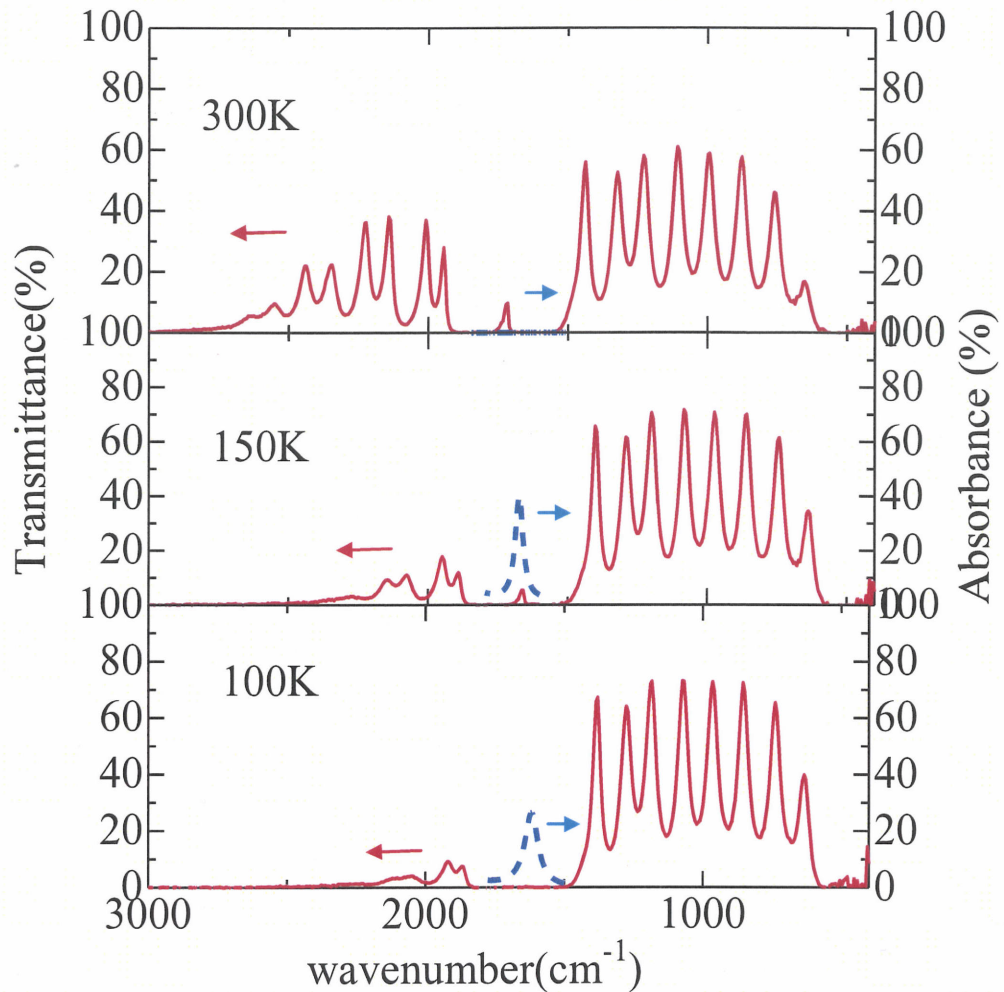

Figure 5.8 Temperature dependence of experimental transmission spectrum of VCSEL structure. The resonance peak was damped with the temperature decrease. The blue dashed line shows theoretical absorbance in resonant region.

5.7 Etching technique for device fabrication

Etching process is necessary to fabrication injection type laser. The device structure is schematically shown in Figure 5.9. Indium was used as contact electrode for contact. Four different method of device fabrication has been developed in the recent years:

- Cleaving

- Wet chemical etching
- Reactive ion etching(RIE)
- Focused ion beam (FIB) etching.

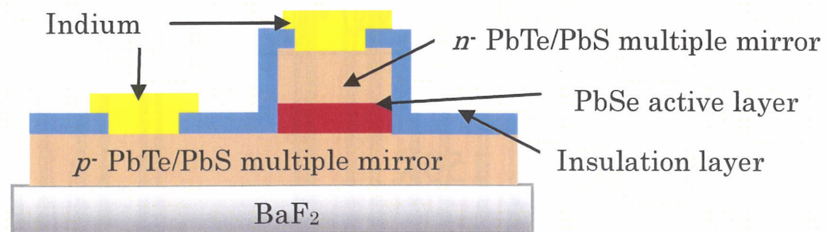

Figure 5.9 Schematic cross-section view of a VCSEL laser structure. Indium is used for the contact electrode.

More suitable for mass production are wet chemical etching and RIE technology. However, these methods show somewhat less promising results and etching technology has to be developed further. RIE can introduce damage to the sample by reactive ions in regions near the surface and this is difficulty in obtaining smooth etched sidewalls (typical roughness 50nm) which are required for device functionality [31]. The disadvantage of RIE is relatively high cost.

Wet chemical etching is an inexpensive way to obtain laser device. No special equipment such as plasma or focused electron beam source is needed. Standard photolithographic procedures are applied to protect specified surface areas with photo resist from etching. In this work we used the wet chemical etching method to fabricate laser device. Two types photoresists were used for the etching process of laser structure as described in Appendix. One is positive photo resist; this resist is removed after development at the exposed areas, while the unexposed resist remains on the substrate after development. Figure 5.10 (a) shows the photography after lithography process using positive photo resist (OFPR800). The resist diameter about 100μm, thickness is about 0.9 μm. Figure 5.10(b) shows 3D photography obtained by confocal laser microscope.

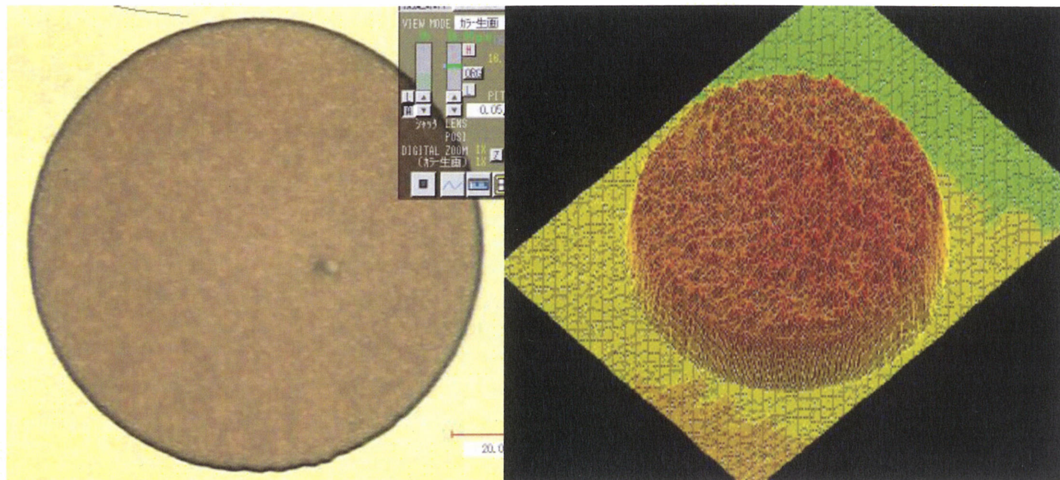

(a) (b)

Figure5.10. Lithography process using positive photoresist. (a) Top view of photoresist, the diameter of dot is about 100 μm. (b) 3D photo of photoresist, the thickness of photoresist is about 0.9 μm.

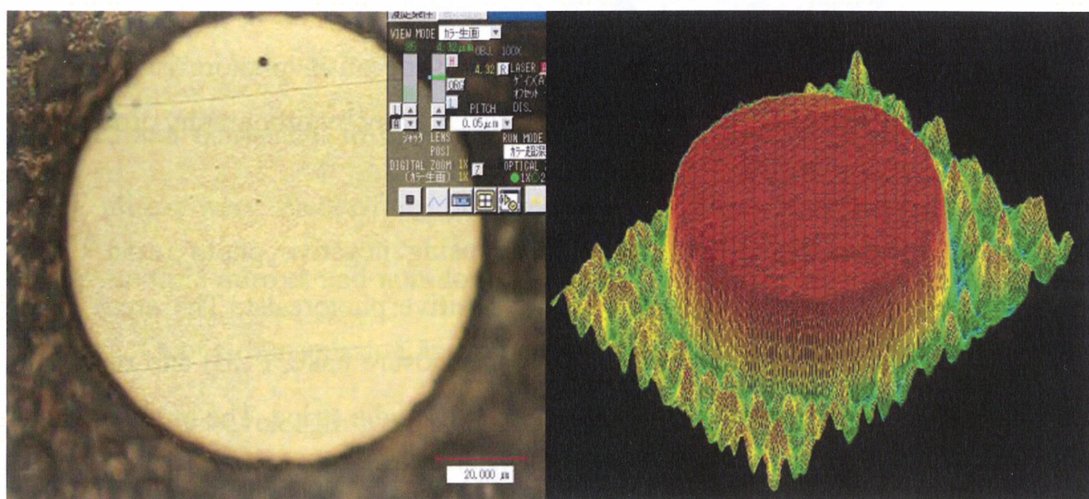

(a) (b)

Figure 5.11 Laser structure after etching by $HBr+Br_2$. (a) top view of laser structure. (b) 3Dmage of laser structure, the etching thickness about 4.2μm.

Figure 5.11 shows the laser structure image after the etching by $HBr+Br_2$ for 40 seconds and its 3d image. From this figure, we can clearly see that diameter of the laser is about 100μm, and etching depth is about 4.2 μm. The side wall of laser structure also very smooth. However, the bottom of sample has considerable roughness. This is due to the etching liquid for the PbTe, did not work well for the PbS layer.

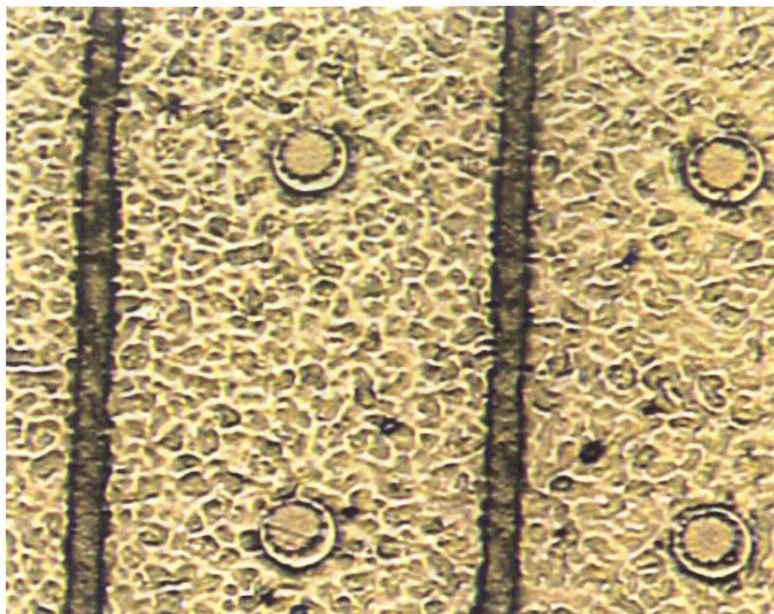

Figure 5.12 Photolithography processes using negative photoresist OMR83 as isolation layer. The circles and stripes were taken away by lithography process.

Figure 5.12 shows photolithography image using negative photo resist OMR83. Negative photoresist behaves opposite to the positive photoresist: The areas exposed crosslink during a subsequent baking step (post exposure bake, PEB) and remain after development. We used the mask including the circles and a stripe. The circle diameter is 80 μm less than the first process, and this is easy to fix the sample. The photo resists thickness about 0.8 μm (the depth profile is measure by optical microscope) as isolation layer for laser structure. Then evaporated indium used as electrode. Figure 5.13 shows photography of laser structure. (a)Using positive resist process to remove indium, (b) shows photography of the lasted process of laser structure; white colour is indium as electrode.

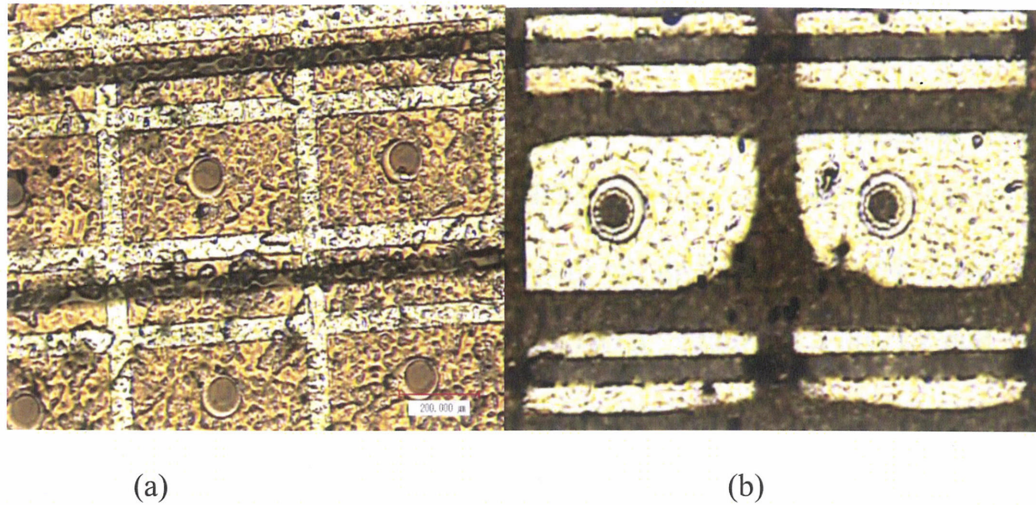

(a) (b)

Fig. 5.13Photolithography process: using positive resist process to remove indium. (a) photography positive resist after development. (b) Photography of lasted laser strucuture, indium as electrode.

5.8 Summary

Up to now, the electrically pumped VCSEL base on IV-VI semiconductor has never been reported. New hot wall epitaxy system for the electrical pumped VCSEL was designed and fabricated. In this system, the p- and n- type high reflectivity PbTe/PbS Bragg mirror were successfully prepared. The VCSELs structure consists of p- and n-type multiple mirrors and non-doped PbSe as active layer were grown on BaF_2 (111) substrate. Optical transmission and reflection spectra of the laser structure designed for 6μm in output wavelength were measured. From the temperature dependence of optical transmission spectra, absorption was observed at 150K as expected from the bandgap of PbSe. To fabricate the laser device, the etching process of grown structure is necessary. Wet-chemical etching method for preparing the laser device was realized.

References

1. Lai F I, Hsueh T H, Chang Y H. Semicond Sci Tech, 2004,(19): L86-L89
2. Zhao L M, Wang Q, Yan C L. Chin J Lasers, 2004, 31(2): 142-144.
3. Hunziker S, Eitel S, Gulden K. SPIE 2001, 4296: 119-126.
4. Ma Y, Wang C, Miao T Q, Opt Precis Engin, 2005, 13: 253-259.
5. Sun Y F, Jin Z H, Ning Y Q, Opt Precis Engin, 2004,12 (5): 449-453.
6. Sale T E. IEE Pro-Optoelectron, 1995, 142 (1): 37-43
7. Iga K. IEEE J Select Topics Quantum Electron, 2000,6 (6): 1201-1214.
8. Winston D W, Hayer R E. IEEE J Quantum Electron, 1988,34 (4):707-715
9. Piprek J, Troger T, Schroter B, IEEE Photon Tech Lett, 1988, 10 (1): 81-83.
10. Liu Y, Ng W C, Choquette K D, IEEE J Quantum Electron ,2005,14(1):15-25
11. Jewell J L, Huang K F, Tai K, et al. Appl. Phys. Letter 1989, 55: 424-426.
12. Koch S W, Jahnke F, and Chow W W, Semi. Sci. Technology 1995, 10: 739-751.
13. Blum O. In, Miller A, Ebrahimzadeh M, Finlayson D M, Semiconductor Quantum Optoelectronics, Institute of Physics Publishing, London, 1999, pp 265-294.
14. Li H and Iga K, Vertical Cavity Surface Emitting Laser Devices, Springer Verlag, Berlin, 2003.
15. Wgutajer T. Compound Semiconductors, 1998, Winter II: 18-29.
16. Redwing J M. Loeber D A S, Anderson N G, et al, Appl. Phys. Letter, 1996,69:1-3.
17. Krestnikv I L. Lundin W V, Sakharov A V, et al, Appl. Phys. Letter, 1999,75:1192-1194.

18. Koeth J, Dietrich R, and Forchel A, Appl. Phys. Letter, 1998,72:1638-1640.

19. Baba T, Yogo Y, Suziki K, Koyama F, and Iga K.Electron Letter, 1993,29:913-914.

20. Heiss W, Schwarzl T, Roither J, et. al. Prog. Quantum Electron 2001, 25:193-228.

21. Gerard A, Burch J M. Introduction to Matrix Method in Optics, John Wiley and Sons, 1975.

22. Rakic A D, Majewski M L. In: Li H and Iga K: Vertical Cavity Surface Emitting Laser Device, Berlin, 2003, pp 259-301.

23. Boberl M. Heiss W, Schwarzl T, et al. Appl.Phys.Letter 2003, 82:4065-4067.

24. Partin D L. IEEE J Quantum Electron 1988,24:1716-1726.

25. Katzir A, Rosman R, Shani Y. et al. In: Cheo P K (ed) Handbook of Solid State Lasers, Marcel Dekker, New York, 1989, pp 227-347.

26. Springholz G, Shi Z, and Zogg H. In: Liu W K and Santos M B, Thin Films: Heteroepitaxial systems, world scientific, Singapore, 1999,pp 621-688.

27. Ishida A and Fujiyayu H. In: Khokhlov D, Lead Chalcogenides: Physics and Applications Taylor and Francis , New York, 2003,pp 347-396.

28. Springholz G, In: Khokhlov D, Lead Chalcogenides: Physics and Applications Taylor and Francis , New York, 2003,pp 123-207.

29. Partin D L and Heremans J. In: Mahajan handbook on Semiconductors Vol. 3a North Holland, Amsterdam 1994, pp 369-450.

30. Feit Z, Kostyk D, Woods R J, and Mak P. Appl. Phys. Letter 1991,58:343-345.

31. F. Ren et al., Journal of Electgronic Materials 1997, 26,1287.

32. Schwarzl T, Heiss W, Springholz G, et al. Phys.Rev. B 2002,65: 245321-9.

33. Schwarzl T, Heiss W, Springholz G, Electron Letter, 2000, 36: 322-324.

34. Springholz G, Schwarzl T, Aigle M, Appl Phys Lett., 2000, 76:1807-1809.

35. Shi Z, Xu G, Mccann P J, Appl Phys Letter, 2000, 76:3688-3690.

36. Heiss W, Schwarzl T, Springholz G, Appl Phys Letter, 2001, 78:862-864.

37. Furst J, Schwarzl T, Boberl M, Appl Phys Letter, 2004,40:966-968.

38. V. Lucarini, J J Saarinen, K. Peiponen and E. M. Vartiainen, Kramers-Kronig relations in optical materials research, Springer, 2005.

Chapter 6
Infrared detectors

6.1. Introduction

Looking back over the past 100 years we notice that IR itself was unknown until 200 years ago when Herschel's experiment with thermometer was first reported. He built a crude monochromattor that used thermometers as a detector so that he could measure the distribution of energy in sunlight. In April 1800 he wrote [1]: *thermometer No.1 rose 7 degrees in 10 minutes by an exposure to the full red colored rays. I drew back the stand ... thermometer No.1 rose, in 16 minutes, 8.375 degrees when its center was 0.5 inch out of the visible rays.*

The early history of IR was reviewed about 40 years ago in two well-known monographs [2, 3]. The most important steps in development of IR detectors are the following:

- In 1921 Seebeck discovered the thermoelectric effect and soon thereafter demonstrated the first thermocouple.
- In 1929 Nobili constructed the first thermopile by connecting a number of thermocouples in series[4],
- In 1933 Melloni modified thermocouple design and used bismuth and antimony for it [5].

Langley`s bolometer appeared in 1880 [6]. Langley used two thin ribbons of platinum foil, connected so as to form two arms of a Wheatstone bridge. Langley continued to develop his bolometer for the next 20 years (400 times more sensitive than his first

efforts). His latest bolometer could detect the heat from a cow at a distance of a quarter of mile. Thus, at the beginning the development of IR detectors was connected with thermal detectors.

The photodetectors were developed in 20th century. The first IR photo- conductor was developed by Case in 1917 [7]. In 1933 Kutzscher at university of Berlin, discovered lead sulphide (from natural galena found in Sadinia) was photoconductive and had response to about 3μm [8].

Many materials have been investigated in the IR filed. Observing a history of the development of the IR detector technology, a simple theorem, after Norton [9], can be stated: *all physical phenomena in the range of about 0.1-1 eV can be proposed for IR detector.* Among these effects are: thermoelectric power (thermocouples), change in electrical conductivity (bolometer), gas expansion (Golay cell), pyroelectricity (pyroelectric detectors), photon drag, Josephson effect (Josephoson junctions , SQUIDs), fundamental absorption (intrinsic photodetectors), impurity absorption (extrinsic photodetectors), low-dimensional solids (superlattice (SL) and quantum well (QW) detectors, different type of phase transitions, etc.

Fig.6.1 gives approximate dates of significant development efforts for the materials mentioned. The years during World War II saw the origins of modern IR detector technology. Interest has centered mainly on the wavelengths of the two atmospheric windows 3-5 and 8-12μm, though in recent years there has been increasing interest in longer wavelengths stimulated by space applications [10].

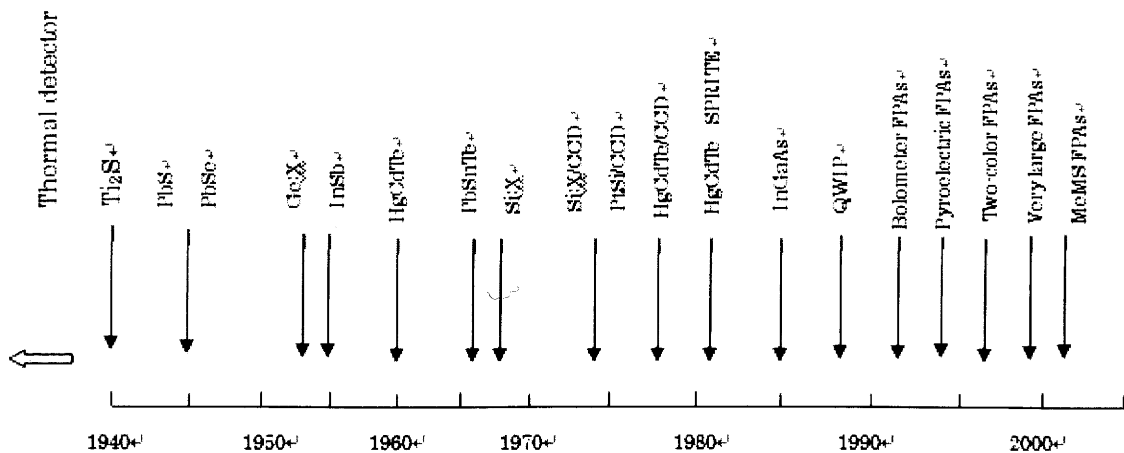

Figure 6.1 History of the development of IR detectors.

6.2 Classification of IR detectors

Progress in IR detector technology is connected mainly to semiconductors, which are included in the class of photo detectors. In this class of detectors the radiation is absorbed within the material by interaction with electrons. The observed electrical output signal results from the changed electronic energy distribution. The photon detectors show a selective wavelength dependence of the response per unit incident radiation power. They exhibit both perfect signal-to-noise performance and a very fast response. But to achieve this, the photon detectors require cryogenic cooling. Cooling requirement are the main obstacle to the more widespread use of IR systems based on semiconductor photodetectors making them bulky, heavy, expensive and inconvenient to use. Depending on the nature of interaction, the class of photon detectors is further sub-divided into different types. The most important are: intrinsic detectors, extrinsic detectors, photo emissive (metal silicide Schottky barriers) detectors, and quantum well detectors. Table 6.1 shows the comparison of various IR detectors.

The second class of IR detectors is composed of thermal detectors. In a thermal detector the incident radiation is absorbed to change temperature of the material, and the resultant change in some physical properties is used to generate an electrical output. The detector is suspended on lags which are connected to the heat sink. The signal does not depend upon the photonic nature of the incident radiation. Thus, thermal effects are generally wavelength independent; the signal depends upon the radiant power but not upon its spectral content. Thermal detector typically operates at room temperature. They are usually characterized by modest sensitivity and slow response, but they are cheap and easy to use. They have found widespread use in low cost applications, which do not require high performance and speed.

Table 6. 1 Comparison of IR detectors (Ref.[11])

Detector type	advantages	disadvantages
Thermal	light, rugged, reliable and low cost room temperature operation	Low detectivity at high frequency Slow response (ms order)
Photon intrinsic		
IV-VI	available narrow-gap Materials well studied	Poor mechanical Large permittivity
II-VI	Easy band-gap tailoring Well-developed theory and experiment Multicolor detectors	non-uniformity over large area, High cost in growth and processing

Since the initial proposal by Easki and Tsu [12] and the advent of MBE, the interest in semiconductor superlattice and quantum well structure has increased continuously over

the years, driven by technological challenges, new physical concepts and phenomena as well as promising applications. Many case of quantum well infrared detector based on intersubband absorption was report, the material such as GaAs/AlGaAs, InGaAs/InAlAs, InAs/GaInSb and so on. However, IV-VI semiconductor detector based on intersubband absorption has never reported. Our group found strong intersubband absorption in short-period EuTe/PbTe double well superlattice at normal incidence [13]. In this chapter, we will describe the intersubband absorption of EuTe/PbTe quantum cascade structure at normal incidence suitable for infrared detector and resonant cavity enhanced detector using Bragg mirrors.

6.3 Introduction of Photovoltaic infrared detector based on intersubband absorption

A question arises concerning the motivation for studying quantum well infrared photodetector (QWIPs). After all, technologies based on IV-VI group interband and HgCdTe and InSb are well developed for IR detection and imaging in the wavelength region of about 3-14 μm. The first and foremost important advantage relates to the availability of a mature material and processing technology for QWIPs. With the mature technology, it is anticipated that the cost of an imaging device based on a QWIPs would be substantially less than that based on HgCdTe or InSb, and that a large volume production capability can be easily established [22]. Other advantages relate to the uniqueness and the flexibility of the QWIPs approach, *e.g.*, in high speed and multicolor application.

Most QWIP studies so far concentrated on the photoconductive detection mechanism,

where photon excited carriers are swept out of the quantum well (QW) region by an externally applied electric field. A different class of QWIP structures is formed by devices with built-in inversion asymmetry acting as an internal filed; the device can in principle be operated without external bias voltage. At first sight, this concept has the advantage of a vanishing dark current, such that no generation-recombination noise is present under dark conditions. However, the photocurrent of these photovoltaic QWIPs is associated with much smaller gain by comparison to photoconductive QWIPs. Therefore, photoconductive QWIPs are preferable for applications which require high responsivity, e.g., for sensors operating in the atmosphere windows region. Photovoltaic QWIPs will be a good choice if the integration time of the FPA is limited by the storage capacity of the readout circuit.

Early device concepts for photovoltaic QWIP like structures are shown in Fig.6.2 *a* and *b*. the device reported by Kastalsky *et al.* [17] relies on inter-miniband absorption in a superlattice with an adjacent barrier layer. While electron motion in the lower miniband is blocked by this barrier, electrons excited into the upper miniband gain enough energy to traverse this barrier, thus giving rise to a photocurrent already without external bias voltage. Goossen et al. [18] reported different approach, in which the capacitance of the device is influence by carriers emitted into a depletion layer located between an n-type QW and a surface metallization. The asymmetrically doped double-barrier QW structure depicted in Fig. 6.2c and gives rise to an efficient transport mechanism. The general concept

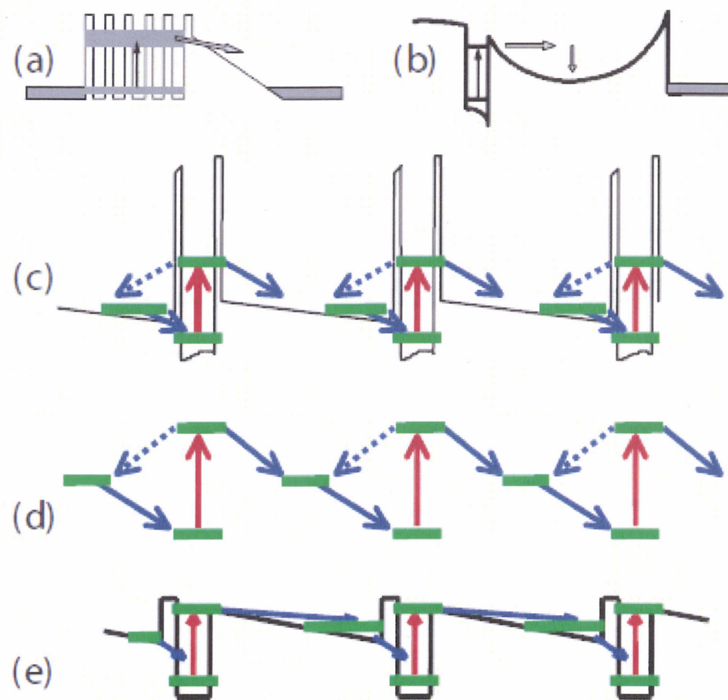

Figure 6.2 Transport mechanism (arrows) of photovoltaic infrared detectors involving intersubband transitions: (a) superlattice with blocking barrier. (b) Single quantum well with surface depletion layer. (c) Asymmetrically doped double- barrier quantum well. (d) General subband configuration for photovoltaic detection, and (e) modulation-doped single barrier quantum well.

behind this transport mechanism is characterized by the configuration of subband level shown in Fig. 6.2d, which forms the basis for the photovoltaic QWIP structures. As a first application of this concept, it is straightforward to conceive of a detector similar to Fig.6.2c, but with reduce barrier heights. This idea leads to the single-barrier QW of Fig.6.2e. Recently a configuration similar to Fig.6.2 e was reported [19] by generating the built in filed by a digitally graded superlattice barrier rather than modulation doping. The photovoltaic effect was successfully achieved. However, this "quantum cascade detector" (the band diagram actually resembles a quantum cascade laser) showed

limited performance due to dark currents cause by residual carrier leakage into resonant states of the barrier.

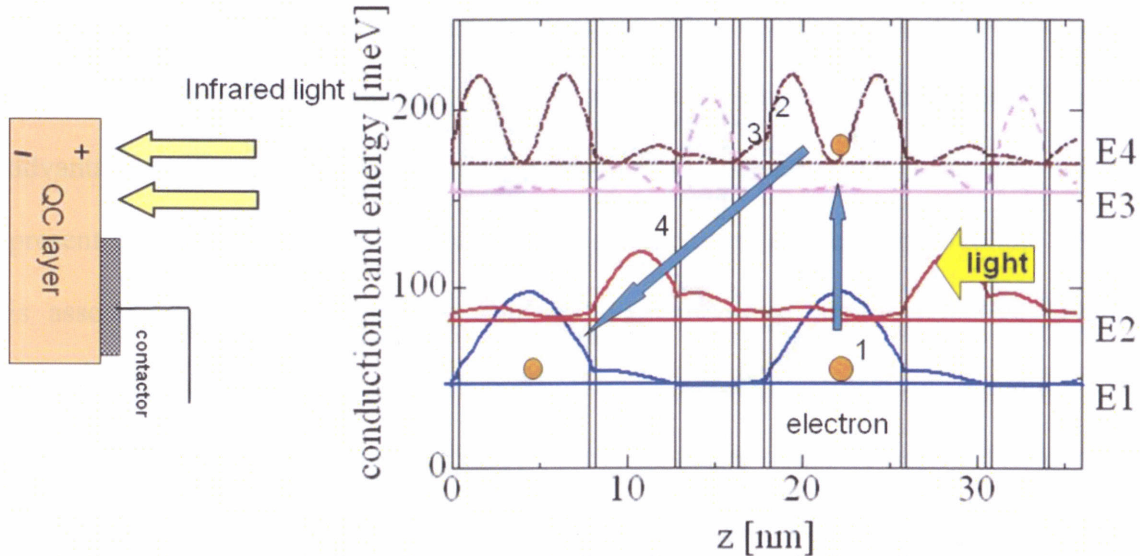

Figure 6.3 Schematics of the four-zone approach for photovoltaic intersubband photo detection.

A similar detectivity as for photoconductive QWIPs has been achieved for photovoltaic detection by using the concept of the "four-zone" [20, 21]. Here each period of the active QWIP region is divided into four zones which can be optimized independently as show in Fig. 6.3. In the excitation zone, carriers are optically excited and emitted into the quasicontinuum above the band edge of the drift zone. A photocurrent without external bias voltage is achieved, if the excited carriers relax into the capture zone. Finally, the carriers have to cross the tunneling zone in order to populate the adjacent QW. In this work, intersubband absorption in EuTe/PbTe quantum cascade structure was studied at normal incidence. Since intersubband absorption in III-V semiconductor is not observed at normal incidence; it has a merit in the device design.

6.4 Intersubband absorption in EuTe/PbTe quantum cascade structure

EuTe/PbTe multiple quantum wells superlattices were prepared by hot wall epitaxy with PbTe, Eu, and Te as source materials. Cleaved KCl (100) was used as the substrate. Bi_2Te_3 dopant as a donor impurity in the growth equipment, all grown sample were n-type. The background in the growth chamber was about $5*10^{-7}$ Torr by ULVAC UTM-500 turbo molecular pump during growth. The source temperatures were 550℃ for PbTe, 450℃for Eu and 300℃ for Te. The substrate temperature was 260℃.The growth rate of the PbTe was 1.5nm/s. The sample structure prepared was 200 periods of monolayer EuTe/7.5nm PbTe/monolayer EuTe/4.5nm PbTe/monolayer EuTe/3nm PbTe/monolayer EuTe /1.5nm PbTe grown on KCL (100) substrate with 2.5μm PbTe buffer layer. Total thickness of thin film is about 6μm. X-ray diffraction (XRD) was employed to characterize the quality of the sample structures by Rigaku RINT Ultima III diffract meter, and Cu ($K\alpha_1$, $K\alpha_2$) radiation was used as the X-ray source. Room temperature (RT) and Low temperature (LT) optical transmission spectra were measured by FTIR spectrometer (Jasco FTIR). The film thickness was calculated from the optical transmission spectrum.

X-ray diffraction for the sample in 2θ-θ measurement is shown in Fig.6.3. Satellite peaks are observed at the angles which satisfy the Bragg condition $2D\sin\theta = n\lambda$ (D: one period thickness of quantum cascade structure, n: integer) and the intensities are simply calculated as the square of the absolute value of summation of scattering amplitudes from all the atomic layers of the quantum cascade structure. The theoretical

values are also shown with the dashed line in Fig. 6.4. A very good agreement between the theoretical and experimental results was obtained, which shows good controllability of the quantum cascade structure with the Hot Wall Eptitaxy (HWE) system.

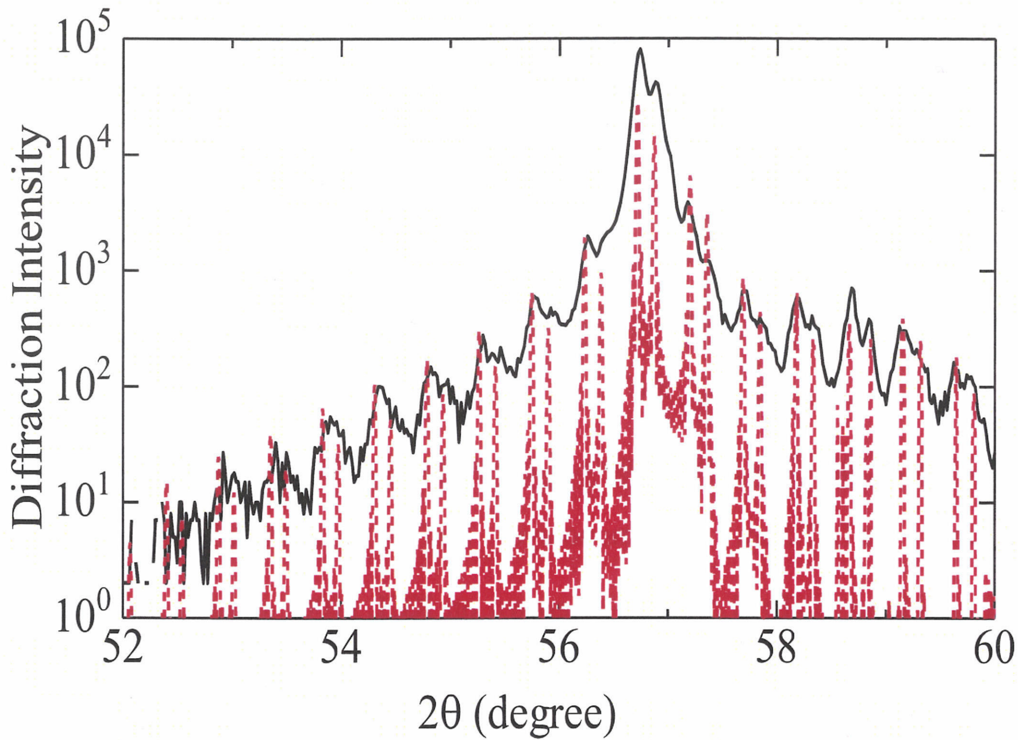

Figure 6.4: Experimental (solid line) and simulated (dished line) X-ray diffraction patterns of EuTe/PbTe QC structure.

Figure 6.5 shows the subband structure calculated for the sample. In this calculation, band-edge effective masses in PbTe was assumed to be $m_l = 0.41m_0$ and $m_t=0.041m_0$, which give good agreement between experimental and theoretical intersubband absorption edges in PbTe -based superlattices at room temperature . The effective mass of EuTe was assumed to be $0.4m_0$ and band offset was assumed to be $\triangle E_C =$ 1000 meV. Energy band structures were calculated for the sample by envelope function approximation. In narrow direct gap semiconductors, the E-*k* relationship near the bottom of conduction band has a large nonparabolicity due to the mixing of core states

in valence band top and conduction band bottom[14,15], thus , the orthogonality of envelope functions can be broken and transition element get non zero value of transition probability.

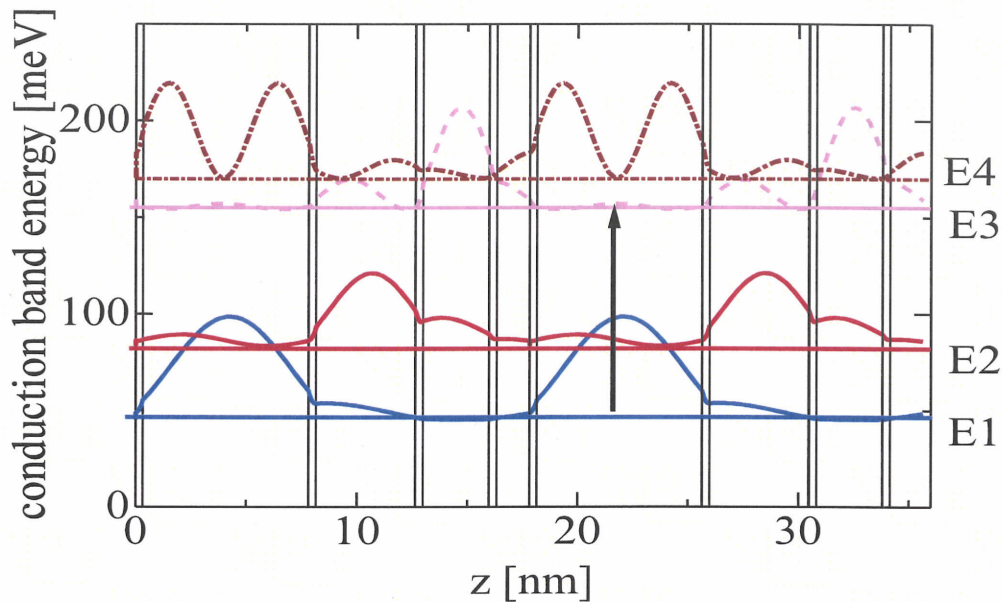

Figure 6.5: Subband structures for EuTe/PbTe QC structure, calculated by envelope function approximation. Absorption position indicated by arrows.

Optical transmission properties were measured by FTIR spectrometer for sample at normal incidence and the results are shown in Figure 6.6 with absorption coefficients obtained by simulation and different temperature. In the simulation, we assumed Lorentian-shape ISB absorption and free carrier absorption proportional to the wavelength squared. The blue lines shown absorption coefficient of sample obtained by simulation. The arrow indicates the theoretical value of intersubband transition obtained form subband calculations. The absorption position shifts to high energy side with the temperature decrease owing to a large temperature dependence of PbTe the effective masses. The band gap decrease strongly with the decreasing temperature. The proportion of effective mass to the band gap in PbTe shifted the intersubband transition

energy to the higher energy side with decreasing temperature. This structure gives the possibility of fabrication of novel devices, such as intersubband image sensor at normal incidence.

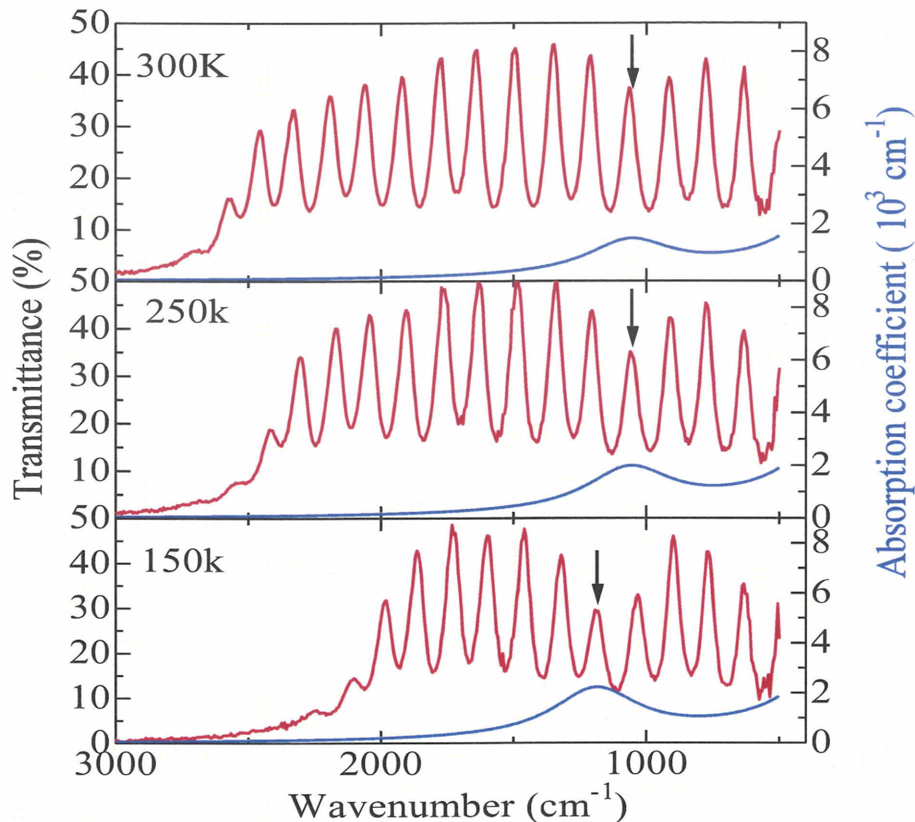

Figure 6.6: Temperature dependence of optical transmission spectra and absorption coefficients (blue line). Intersubband absorption position shifted to high energy side owing to the temperature dependent effective masses in PbTe. Arrows show theoretical absorption positions.

6.5 Resonant cavity enhance detector structure base on IV-VI semiconductors

6.5.1 Design of RCD

The aim of this section is to describe mid-IR photo detectors which are selectively

sensitive to a specific narrow wavelength range. Resonant cavity detectors (RCDs) are optoelectronic devices whose performance is enhanced by placing the active device structure inside a Fabry-Pérot resonant cavity. Such devices benefit from the wavelength selectivity and the large increase of the resonant optical field in the cavity. Off-resonance wavelengths $\lambda \neq \lambda_0$ are rejected by the cavity. Photo detector structures based on RCD can have very thin active layers [16]. This yields higher directivities (smaller volume where noise carriers are generated), and, in addition, to faster devices. Moreover, high quantum efficiencies η result because the photon may be reflected many times before it is absorbed in the thin active layer. And RCD have major advantage compared to the use of a band pass filter in front of a conventional detector. Quantum efficiencies close to unity can be achieved even for very thin absorber layers. Due to the multiple possible passes of a photon inside the cavity until it is absorbed. Therefore the volume where generation recombination noise and diffusion currents are generated is smaller compared to a conventional photo diode, while the quantum efficiency remains high. This results in an improved noise limit. Here are described resonant cavity diodes with resonant wavelength λ in the 5 to 7 μm wavelength range. Figure 6.7 shows band structure of active layer structure of RCDs. In PbSe active layer, carriers flow by diffusion. On the other hand, carriers flow by electric field in the depletion layer, resulting in fast response time, in the PbSrSe/PbSe DH active layer.

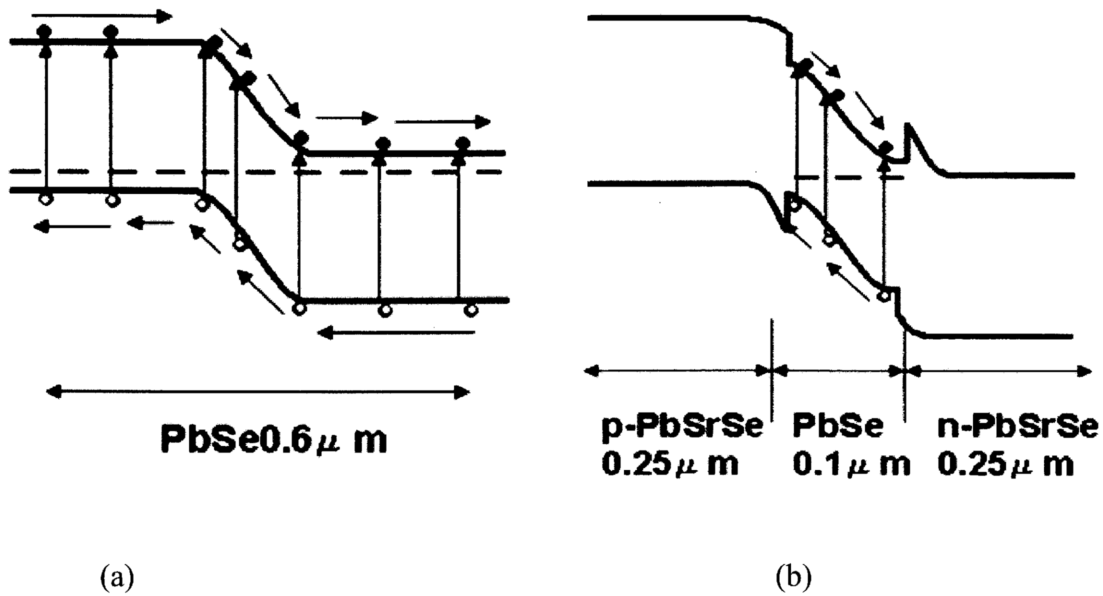

(a) (b)

Figure 6.7 Band structure of RCD active layer. (a) PbSe active layer. (b) PbSrSe/PbSe DH active layer.

We also compared theoretical optical properties of RCD structures with PbSe active layer and with PbSrSe/PbSe/PbSrSe DH active layer at 90K as shown in Fig. 6.8. Dashed lines show absorption coefficients in active layers. For RCD with PbSe (thickness is 700nm) active layer, the absorbance is about 30% at resonant center, and the transmittance peak was damping at resonant region. For RCD structure with PbSrSe/PbSe/PbSrSe DH active layer, the absorbance is about 40% at resonant center with sharp resonant line, and resonant peak still is not damping with narrow line width.

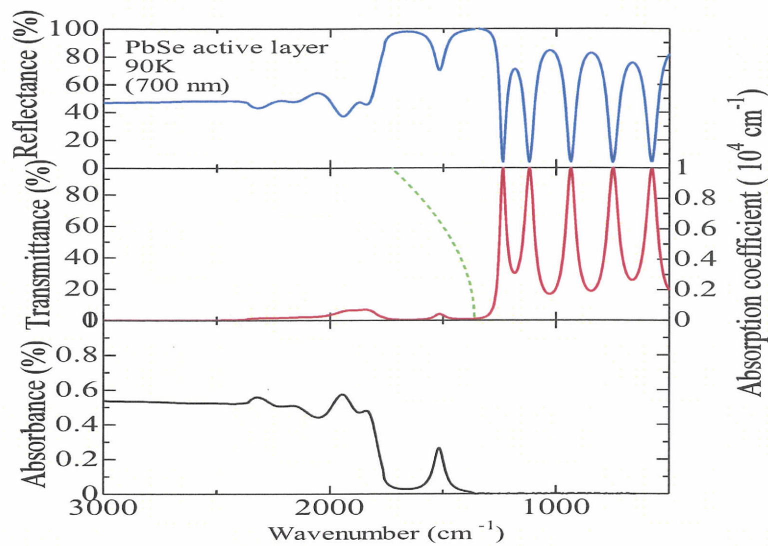

(a)

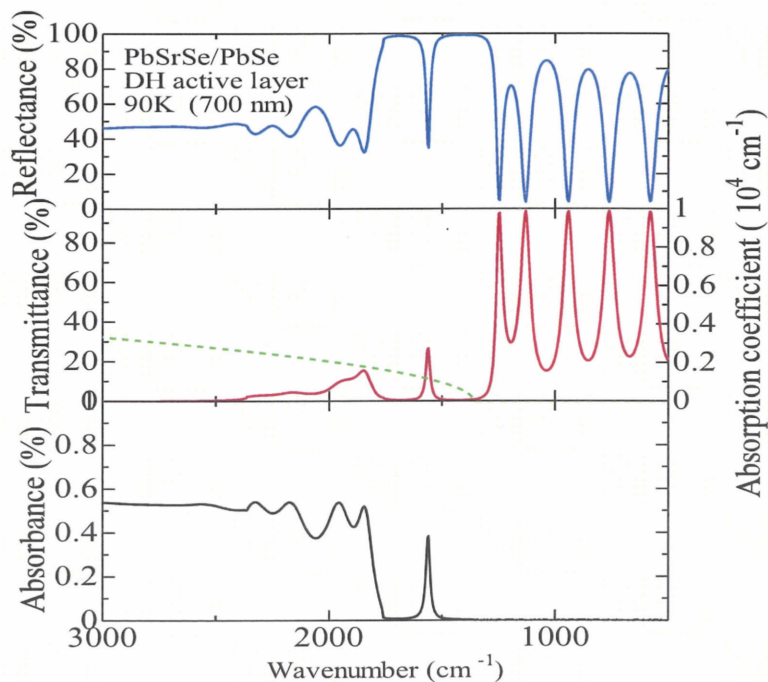

(b)

Figure 6.8 Calculated of optical reflectance, transmittance, and absorbance for different active layer RCD structures at 90K, (a) PbSe (thickness is 700nm) as active layer, the absorbance is about 30% at resonant center. (b) PbSrSe/PbSe/PbSrSe DH as active layer, the absorbance is about 40% at resonant center, and resonant peak still not damping with narrow line width.

6.5.2 Fabrication of RCD

As a Fabry-Perot resonator, a resonant cavity detector consists of a cavity embedded between two mirrors. Both the mirror must be non-absorbing at the target wavelength and the reflectivity of the mirrors has to be high. A schematic drawing is shown in Figure 6.9. Bragg mirrors are used for high reflectance with thicknesses of the individual layers $d=\lambda/4n$. The PbTe and PbS film property same with chapter 5.

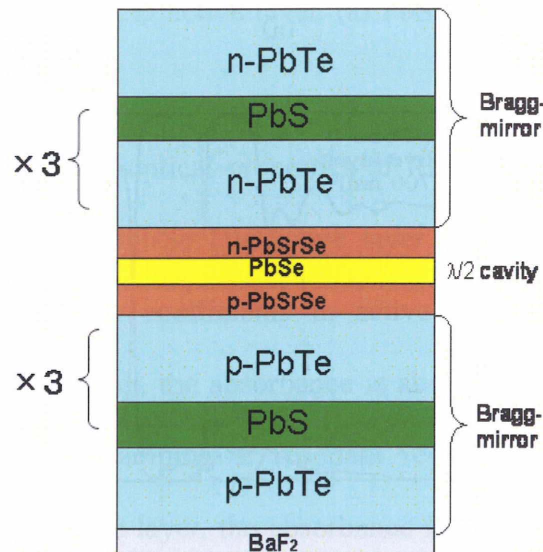

Figure 6.9 Schematic of RCED structure.

Figure 6.10 shows the target wavelength about 6μm RCD optical property with varies temperature. Top and bottom mirror consist of (PbTe (0.27μm) and PbS (0.37 μm))* 3 periods +PbTe (0.27μm). In order to block unnecessary modes, material properties of the absorbing layer may be changed. By adding Sr to the PbSe absorbing layer, a shift of the cut off wavelength occurs. Resonant cavity consists of n-PbSrSe 0.25μm PbSe

0.1μm, p-PbSrSe 0.25μm as active layer and the mirror reflectance at the target wavelength is more than 99%. The reflectance spectrum (blue line) was also calculated. We also considered the free carrier absorption in the mirror during theoretical calculation. Transmission spectra measurement of the completed RCD structure was made at varies temperature from 300 K to 90K. The possibility to obtain a photovoltaic detector with sensitivity only within a narrow wavelength range at any desired wavelength in the mid-infrared rang is the advantage of this type of device.

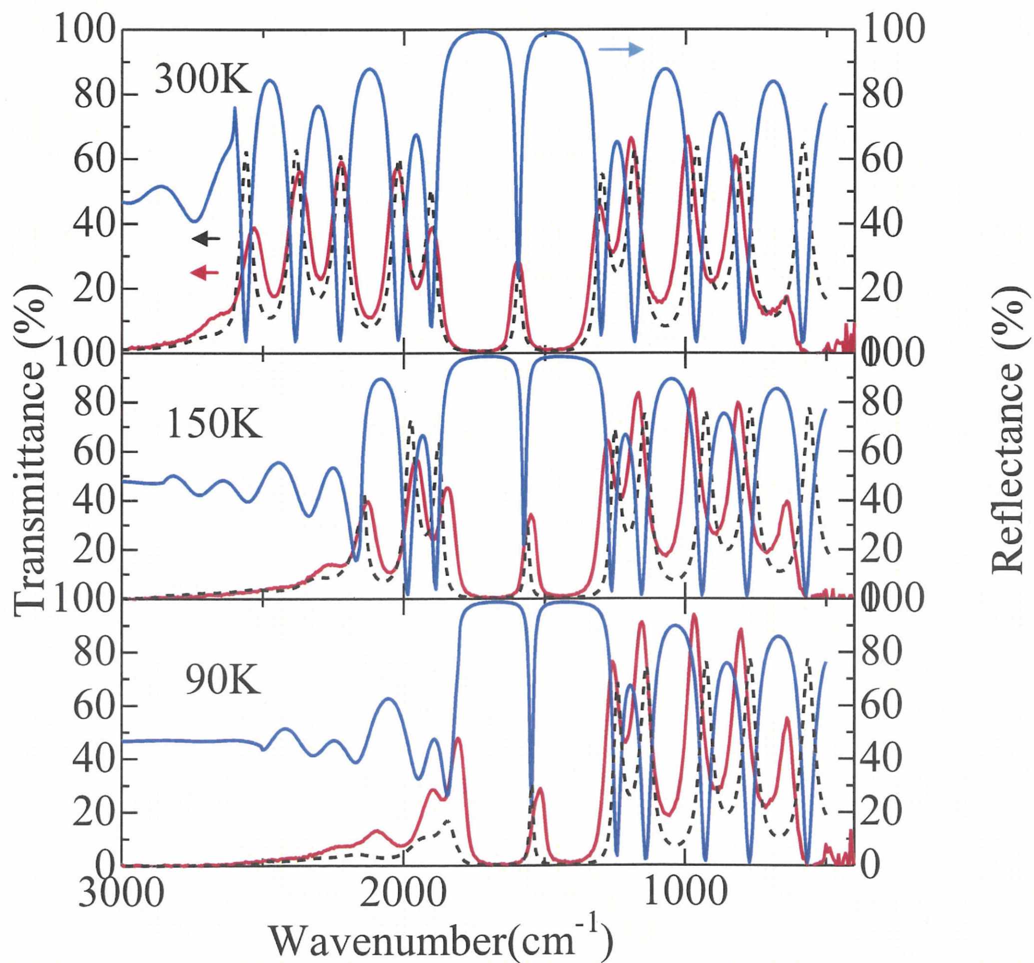

Figure 6.10. Optical properties of RCD structure. The theoretical transmission (dashed line) and reflection spectra (blue line) were calculated.

6.6 summary

EuTe/PbTe quantum cascade structures were deposited on KCl (100) substrate by hot wall epitaxy system. XRD measurements of the structure exhibited many satellite peaks, which confirmed a high quality of EuTe/PbTe quantum cascade structure. Intersubband absorption in this structure was observed at the room temperature in normal incident transmission spectrum measured by FTIR. This structure has the possibility to apply for an intersubband image sensor at normal incidence.

Resonant cavity detector (RCD) structure, which has sensitivity for special wavelength designed, was also proposed using the n-PbSrSe -PbSe-p-PbSrSe active region between *p-, n-* PbTe/PbS multiple resonator. Optical transmission spectra of the RCD structure have been measured and discussed.

References

1. W. Herschel, Philos. Trans. Roy.Soc. London (1800) 284.

2. R. A. Smith, F.E. Jones, R. P. Chasmar, The Detection and measurement of Infrared Radition, Clarendon, Oxford, 1958.

3. P. W. Kruse, L. D. McGlauchlin, R. B. Mcquistan, Elements of Infrared Technology, Wiley, New York, 1962.

4. E. S. Barr, Historical survey of the early development of the infrared spectral region, Am. J. Phys. 28 (1960) 42-54.

5. E.S. Barr, Infrared Phys. 2 (1962) 67-73.

6. E. S. Barr, Infrared Phys. 3 (1963) 195-206.

7. T. W. Case, Phys. Rev. 9 (1917) 305-310.

8. R. J. Cushman, Film-type infrared photoconductors, Proc. IRE 47 (1959) 1471- 1475.

9. P. R. Norton. Infrared detectors in the next millennium, Proc. SPIE 3698 (1999) 652-665.

10. A. Rogalski, Infrared detectors, Gordon and Breach Science Publishers, Amsterdam, 2000.

11. M. Razegi, Current status and future trends of infrared detector, Opto-Electron. Rev. 6 (1998) 155-194.

12. L. Esaki, R. Tsu, IBM Joural of Research and Development ,1970, 14, pp 61-65.

13. A.Ishida, M. Veis, Y.Inoue, Jpn. J. App. Phys., 2007, 46, pp L281-L283.

14. D. L. Mitchell, S. S. Schad, H. Wu, W. J. Schaff, and L. F. Eastmand, Appl. Phys. Letter, 2003, 83, 572.

15. M. Kriechbaum, K.E. Ambrosch, E. J. Fantner, H. Clemens, and G. Bauer, Phys. Rev. B, 1984, 30, 3394.

16. H. Zogg, M. Arnold, D. Zimin, K. Wiesauer, G. Springholz, Appl. Phys. Letters, 2003, 82, p4065.

17.M.Ershov, C. Hamaguchi, V. Ryzhii, Jpn, J. Appl. Phys. 1996, 35,1395.

18. K. W.Gossen, S.A.Lyon, J. Appl. Phys. 1988,63,5149.

19.L.Gendron, M. Carras, A. Huynh, V.Ortiz, C.Koeniguer, V.Berger, Appl. Phys. Letter, 2004, 19,347.

20.H.Schneider, C. Schonbein, M. Walther, K. Schwarz, J. Fleissner, P. Koidl, Appl. Phys. Letter, 1997,71,246.

21.H. Schneider, C.Schonbein, S.Ehret, R. Rehm, M.Walther, K. Schwarz, J. Flessner, P.Koidl, ECS Proc. 1997,97-33, 180.

22.H.Schneider, H.C. Liu, “quantum well infrared photodetectors: physics and applications” Springer, 2007,chapter 5,pp96-108.

Chapter 7
Conclusions

This work has been dedicated to the growth of IV-VI semiconductors for optical device application. PbTe and PbS were used as materials to prepare *p*- and *n*- type Bragg mirrors for electrically pumped VCSEL and RCD applications. The optical transmission properties of the VCSEL and RCE structures were measured to confirm the growth of designed structures.

New hot wall epitaxy system for electrical pumped VCSEL was designed and fabricated. In this system, high quality p- and n- type high reflectivity PbTe/PbS multiple mirror were successfully prepared. The VCSELs structure consists of p- and n-type multiple mirrors and non-doped PbSe as active layer were grown on $BaF_2(111)$ substrate. Optical transmission and reflection spectra of the laser structure designed for 6μm in output wavelength were measured. From the temperature dependence of optical transmission spectra, absorption at resonant wavelength (6μm) was observed at 150k as expected from the bandgap of PbSe. To fabricate the laser device, the etching process of growth structure is necessary. Wet-chemical etching method for preparing the laser device was realized.

EuTe/PbTe quantum cascade structures were deposited on KCl (100) substrate by hot wall epitaxy system for mid-infrared detector application. XRD measurements of the structure exhibit many satellite peaks, indicating a high quality of EuTe/PbTe quantum cascade structure. Strong intersubband absorption in this structure was observed in the room temperature transmittance spectra measured by FTIR at normal incidence.

Resonant cavity detector (RCD) structure based on the n-PbSrSe -PbSe-p-PbSrSe active layer sandwiched with p- and n- PbTe/PbS Bragg mirrors was proposed and prepared. Transmission spectra of the RCD structure were measured at varies temperature. Optical transmission spectra were compared with theoretical value and good agreement, which shows the growth of high quality RCD structure was obtained. In theoretical calculation, high sensitivity and narrow line width detection were expected for the DH active structure compared with PbSe thick active layer.

Appendix Photolithography procedure

Positive photoresist process (OFPR-800)

1	HMDS		3000rpm	60sec
2	Oven	80℃	3min	
3	OFPR800		3000rpm	50sec
4	Oven	80℃	20min	
5	Exposure		3sec	
6	Draw NMD-3		23℃ (RT)	30sec
	Pure water			30sec
7	spin dry			
8	Post baking oven		120℃	30min

Negative Photoresist Process (OMR83)

1	HMDS	3000rpm	60sec		
2	Oven	80℃	3min		
3	OMR83	3000rpm	50sec		
4	Oven	80℃	20min		
5	Exposure		0.5sec		
6	Draw	develop	23℃ (RT)	30sec	
	Rinse		30sec		
7	spin dry				
8	Post baking oven		120℃	30min	

Acknowledgement

First of all, I am deeply indebted to my supervisor Professor Akihiro Ishida for his help, invaluable guidance and advice. Thank him for offering me the opportunity to perform research at his laboratory for five years.

I wish to thanks to Associate Professor Yoku Inoue for fruitful scientific discussions during my study in Shizuoka University for 5 years.

I would also like to acknowledge all present and former members of the Ishida Lab. Who helped me to make experiments and feel myself comfortable in the laboratory. They are: Hagihara san, Yamano san, Martin Veis san, Yamada san, Tsujiya san, Kobayashi san, yokoyama san Furuhashi san. Especially, Dr. Martin Veis help me to check this thesis.

I wish to thank the numbers of my committee: Prof. M. Tabe, Prof. H. Inokawa, Prof. H. Tatsuoka, and Ass.Prof. Y. Inoue and Prof. A. Ishida. For their careful reading of my thesis and their constructive comments.

I also thanks to Dr. Bo Liang, Dr. Qiang Ma as my friend, share with my foreigner student life in Hamamatsu, Japan.

I would like to acknowledge the financial support of my study and research in japan by the 21st COE program of Nanovision science.

Last, I would like to thank my wife, Dr. Lixin Wang, for support me to get Phd degree. I am grateful to my father , my mather, my borther for their support, understanding and all the help they provided during my work at Shizuoka University.

Publication list

(1) Published paper

- PbTe/PbS Multilayer mirror for EuTe/PbTe surface emitting quantum cascade lasers (Daoshe Cao, Taiki Yamano, Yoku Inoue, Akihiro Ishida) IEEJ Trans.FM 129,11 (2009).
- Seebeck effect in PbTe films and EuTe/PbTe superlattices (Akihiro Ishida,Tohiro Yamada,Daoshe Cao,Yoku Inoue,Matin Veis and Takuji Kita) Journal of Applied physics,106,023718 (2009).
- Seebeck Effect in IV–VI Semiconductor Films and Quantum Wells (Ishida, Akihiro; Cao Daoshe; Morioka, Sinsuke; Inoue, Yoku; Kita, Takuji) Journal of Electronic Materials,38,940 (2009)
- "Enhanced seebeck coefficient in EuTe/PbTe[100] short-period superlattices" (Akihiro Ishida, Daoshe Cao, Sinsuke Morioka, Martin Veis, Yoku Inoue, and Takuji Kita) Appl.Phy.Lett. 92,182105 (2008)

(2) International conference:

- "Intersubband absorption in EuTe/PbTe multiple quantum wells"(Daoshe Cao,Taiki Yamano, Yoku Inoue and Akihiro Ishida) The 10th Takayanagi Kenjiro Memorial Symposium and The 5th International Symposium on Nanovision Science, Hamamatsu, Japan (2008.11.17-18)
- "Semiconductor Quantum Wells for Intersubband Device Applications"(Akihiro Ishida, Daoshe Cao, Martin Veis and Yoku Inoue) The 10th Takayanagi Kenjiro Memorial Symposium and The 5th International Symposium on Nanovision Science, Hamamatsu, Japan (2008.11.17-18)
- "PbTe/PbS Multilayer Mirror for Surface Emitting Quantum Cascade Lasers" (Daoshe Cao, Jun Kumara, Yoku Inoue and Akihiro Ishida) International Quantum Cascade Lasers School & Workshop, 14-19 Sept. 2008, Monte Verita, Switzerland
- "Normal Incident Intersubband Absorptions in EuTe/PbTe Superlattices", (A.Ishida, M.Veis, D.Cao, and Y.Inoue) , 9th Int. Conf. Intersubband Transitions in Quantum Wells, 9-14 Sept. 2007, Ambleside, Cambria, U.K.

(3) Domestic conference：

- "EuTe/PbTe 量子カスケード構造の垂直入射サブバンド間吸収と赤外線検出への応用" (曹道社、山野大樹、井上翼、石田明広) 第 56 回応用物理学関係連合後援会、2009.3.30 筑波大学
- "サブバンド間遷移デバイス応用へ向けた EuTe/PbTe 量子井戸の作製と光学特性" (山野 大樹，曹 道社，石田明広)日本赤外線学会第 18 回研究発表会、2008,10,30-31 神戸
- "PbS 量子ドットを埋め込んだ PbTe 薄膜の熱電特性" (石田明広,曹道社，森岡伸介,井上翼，藤本正之，木太拓志) 第 55 回応用物理学関係連合講演会,2008.3.30 船橋.
- "EuTe/PbTe 超格子の垂直入射サブバンド間吸収 II" (曹道社、ﾊﾞｲｽ･ﾏｰﾁﾝ、森岡伸介、井上翼、石田明広) 第 68 回応用物理学会学術講演会, 2007.9.7 札幌
- "X 線回折による PbTe/PbTeSe 及び EuTe/PbTe 超格子の構造と相互拡散評価" (曹道社, ﾊﾞｲｽ･ﾏｰﾁﾝ, 井上翼, 木太拓志, 石田明広,) 第 67 回応用物理学会学術講演会(2006), 草津.
- "PbTe 薄膜及び EuTe/PbTe 超格子の熱電特性" (石田明広, 曹道社, バイスマーチン, 井上翼, 木太拓志) ,第 67 回応用物理学会学術講演会(2006), 草津.